2021-12

A transient numerical model for desiccant-coated fixed-bed regenerators and compensation for transient sensor errors

Ramin, Hadi

Taylor and Francis

Hadi Ramin, Easwaran N. Krishnan, A. Gurubalan & Carey J. Simonson (2022) A transient numerical model for desiccant-coated fixed-bed regenerators and compensation for transient sensor errors, Science and Technology for the Built Environment, 28:3, 422-442, DOI: 10.1080/23744731.2021.2017236

https://hdl.handle.net/10388/14881

https://doi.org/10.1080/23744731.2021.2017236

A transient numerical model for desiccant-coated fixed-bed regenerators and compensation for transient sensor errors

Abstract

Desiccant-coated fixed-bed regenerators (FBRs) can achieve high effectiveness due to high ratio of energy transfer area to volume, and therefore, they are favourable air-to-air energy recovery exchangers for HVAC systems. However, unlike other types of energy recovery exchangers, the air properties (i.e., temperature and humidity) at the outlet of FBRs vary with time. The variations in outlet airflow properties can cause errors in measurements because the measurements include the FBR and sensors transient responses. In this paper, a numerical model is developed to evaluate the performance of desiccant-coated FBRs and their transient operation. The model consists of an exchanger model (FBR model) and sensor (temperature and humidity) models to distinguish the actual performance of the FBR alone from the measured performance, which includes both the FBR and the sensor's response. The model is validated with experimental measurements and available results in the literature. The model can decouple the measured response of the FBR and sensors to predict the FBR performance. This paper's main contribution is an insight into the complex heat and mass transfer processes in desiccant-coated FBRs and measurement sensors. The results of this paper could be used to provide practical recommendations for humidity measurements of different types of desiccant-coated FBRs developed for HVAC applications. Furthermore, the measurement requirements in the current testing standards (ASHRAE 84 and CSA C439-18 standards) for FBRs are examined. Recommendations from this paper could be implemented in future versions of these standards.

Keywords: Desiccant-coated fixed-bed regenerators (FBRs), humidity measurement, performance evaluations, sensor transient response, test standards (ASHRAE standard 84 and CSA C439-18 standard), and air-to-air energy exchangers.

Nomenclature

A_d	surface area of desiccant, m^2
A_g	cross-sectional area of airflow duct, m^2
A_m	matrix cross-sectional area, m^2
C	constant describing the shape of sorption curve
Cp_m	specific heat capacity of matrix, J/(kg·K)
Cp_g	specific heat capacity of air, J/(kg·K)
C^*	heat capacity rate ratio
Cr^*	matrix heat (or moisture) capacity ratio
Crm^*	matrix moisture capacity ratio
Crm_o^*	overall matrix moisture capacity ratio
H	enthalpy per mass of dry air, kJ/kg
H^*	operating condition factor
$\overline{H}$	average enthalpy over a period, kJ/kg
h	convective heat transfer coefficient, W/(m^2·K)
h_m	convective mass transfer coefficient, kg/(m^2·s)
h_{ad}	heat of adsorption, kJ/kg
h_{fg}	heat of vaporization, kJ/kg
k	thermal conductivity, W/(m·K)
L	length of the heat exchanger, m
$\dot{m}'$	rate of phase change per unit of length, kg/s·m
n	integer
NTU_o	overall number of transfer units
NTU_{mt}	number of moisture transfer units
NTU_{ht}	number of heat transfer units
P	pressure (Pa)
P	complete cycle of FBR, s
P_{cd}	cold and dry period, s
P_{hh}	hot and humid period, s
RH	relative humidity, (%)
RH_s	relative humidity measured by RH sensor, (%)
T	temperature, °C
$\overline{T}$	average temperature over a period, °C
T_m	matrix temperature, °C
T_s	Sensor measured temperature, °C
T^*	dimensionless temperature
t	time, s
t^*	(t/P_h): dimensionless time
u	mass fraction of water in the desiccant, kg/kg
V	mean airflow velocity, m/s
W	humidity ration, kg/kg
W_s	measured humidity ratio by sensor, kg/kg
W_m	desiccant maximum moisture capacity, (kg/kg)
x	axial coordinate, m
x^*	dimensionless distance

Greek symbols

α	thermal diffusivity, m^2/s
Δε	effectiveness error (%)
ΔH_l	latent energy difference between hot/humid and dry/cold inlet conditions (kJ/kg)
ΔH_s	sensible energy difference between hot/humid and dry/cold inlet condition (kJ/kg)
ΔT	temperature difference between hot/humid and dry/cold inlet conditions (°C)
ΔW	humidity difference between hot/humid and dry/cold inlet conditions (kg/kg)
ε	effectiveness (%)
η	distribution of phase change energy between the desiccant and the airflow
ρ_a	dry air density, kg/m^3
ρ_v	water vapor density, kg/m^3
$\rho_{d,dry}$	dry desiccant vapor density, kg/m^3
τ_s	sensor time constant, s
$\tau_{t,int}$	internal temperature time constant of humidity sensor, s
$\tau_{h,int}$	internal humidity time constant of humidity sensor, s
χ	independent variable for numerical solution

ACRONYMS

AAEE	air to air energy exchanger
BSM	Bag sampling method
EX	exchanger
EA	exhaust air
FBR	fixed-bed regenerator
HVAC	heating, ventilating and air conditioning
RA	return air
SA	supply air
OA	outdoor air

Subscripts

ave	average
cd	cold and dry period
d	desiccant
dry	dry properties
g	air mixture (dry air and water vapor)
hh	hot and humid period
ht	dimensionless heat transfer group for regenerators
i	average inlet condition
int	internal
lc	latent effectiveness on cold and dry period
lh	latent effectiveness on hot and humid period
m	matrix
max	maximum
min	minimum
mt	dimensionless mass transfer group for regenerators
o	outlet condition
sh	sensible effectiveness on hot and humid period
sc	sensible effectiveness on cold and dry period
th	total effectiveness on hot and humid period
tc	total effectiveness on cold and dry period
v	water vapor
w	water

1 Introduction

Air-to-air-energy exchangers (AAEEs) are widely used in heating, ventilation, and air conditioning (HVAC) applications because they increase the energy efficiency of HVAC systems by transferring energy/heat between the exhaust airstream (leaving from buildings) and the outdoor fresh supply airstream entering buildings to precondition the supply air (Kassai 2018; Wallin, Madani, and Claesson 2012). Different types of AAEEs are available in the market, including fixed-plate exchangers, heat pipes, energy/heat wheels, fixed-bed regenerators (FBRs), and run-around membrane exchangers (ASHRAE 2012; Diao et al. 2014; Wemhoener et al. 2016; Lowenstein 2008; Fan et al. 2006). Among these AAEEs, FBRs are gaining more interest nowadays for energy recovery in HVAC applications (Borodulin and Nizovtsev 2018; Nizovtsev et al. 2016; Chang, Liang, and Chen 2018; Cerrah, McCague, and Bahrami 2020; Ramin, Krishnan, and Simonson 2019; Ramin et al. 2020), due to their high ratio of energy transfer area to volume, which leads to high effectiveness. In the literature, they are widely referred to as single-core regenerators, double-core regenerators (CSA Group 2018), room-based ventilators (Nizovtsev et al. 2016; Aristov, Mezentsev, and Mukhin 2006), reversing-flow regenerators (CSA Group 2018), and exchangers with a periodic change in the flow direction (Chang, Liang, and Chen 2018; Chang et al. 2013; 2017).

Heat and moisture exchange occurs between the supply and exhaust air streams that alternately flow through the core matrix/s (bed/s) of desiccant-coated FBRs. FBRs are cyclic devices, and each cycle of their operation consists of a hot and humid period and a cold and dry period[1]. Since FBRs operate by storing and releasing heat and moisture, the air properties (i.e.,

[1] FBRs also operate in conditions where heat transfer direction is opposite to moisture transfer. For example, a cool humid night after a rainstorm in dry summer climates. However, for simplicity,periods of FBRs are called hot and cold in this paper. See the definition of H^* in Fig. 3.

temperature and humidity) at the outlet of FBRs continuously change with time. The air properties never reach a steady-state condition; instead, they change in a quasi-steady-state periodic pattern. That is the outlet properties (temperature and humidity) of air streams in FBRs vary with time but cyclically repeat themselves (Ramin, et al. 2020; Krishnan et al. 2020). Figure 1 shows a single-core FBR and its inlet/outlet air temperature/humidity profile for a complete cycle of operation. The variations in the outlet air properties pose challenges for accurate measurement and, consequently, the prediction of latent and sensible effectiveness of desiccant-coated FBRs. These challenges are due to both the transient nature of the air properties at the outlet of the FBR (CSA Group 2018; ASHRAE 2019) and the transient characteristics of sensors(Y. Wang et al. 2007a; 2007b; Dooley and O'Neal 2008). Thus, the measured air properties from sensors during experiments would be different from the actual air properties (ASHRAE 2019; E. N. Krishnan et al. 2020; Ramin, Krishnan, Gurubalan, et al. 2021).

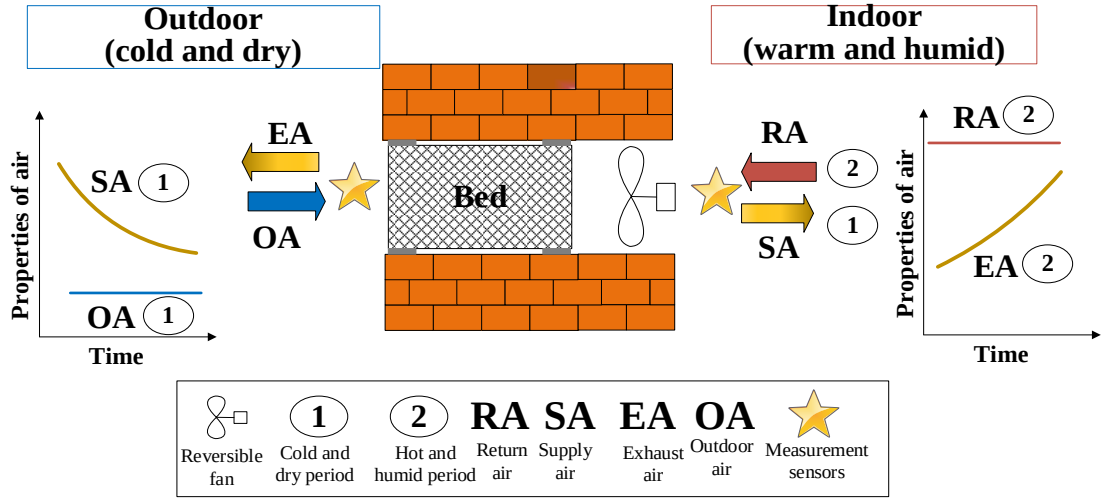

Figure 1. A schematic of single-core FBR and the variation of air properties during discharge and regeneration periods for winter climatic conditions.

Besides the variation of properties during each period, the sensors' conditions in the previous period (which is the initial conditions for the subsequent period) affect the sensor's measurements in the subsequent period. For example, Fig. 1 shows that the sensor located indoors

measuring the outlet air properties during the cold and dry period was previously exposed to the hot and humid indoor air conditions (initial conditions of the sensor). Therefore, both the sensor's initial condition and the variation of airflow properties during each period are critical in obtaining the effect of sensor transient characteristics in the measurement of air properties at the outlet of FBRs (Hashemian 2011; S. Wang, Tang, and Younce 2003; Ramin et al. 2020; Abe et al. 2006; 2006).

The transient characteristics of FBRs and sensors and their impacts on effectiveness measurements of sensible FBRs are documented in the literature. A transient numerical model (Ramin, Krishnan, Gurubalan, et al. 2021) is developed to evaluate the impacts of transient characteristics of sensible FBRs and sensors on the performance evaluation. The model was validated with experimental measurements from a small-scale test facility (Krishnan et al. 2020). In addition, the temperature sensor requirements for an accurate evaluation of effectiveness are recommended (Ramin et al. 2021; Ramin et al. 2020). However, the effects of transient characteristics of desiccant-coated FBRs and sensors on the measurement requirements are not yet studied in the literature. Hence, this study aims to fill this research gap. This study is essential for the accurate evaluation of desiccant-coated FBR's performance. Coupled heat and mass transfer process of desiccant-coated FBRs and temperature-dependent humidity measurement techniques would make their transient characteristics much more complicated compared to sensible FBRs and temperature sensors. Therefore, this paper also provides insights into the coupled response of desiccant-coated FBRs and humidity sensors.

The measurement requirements for testing FBRs have been recently included in ASHRAE standard 84 (ASHRAE 2019) and an affirmative appendix in CSA C439-18 standard (CSA Group 2018). These standards require at least 30 measurements per recovery period (for recovery period

of 60 seconds) with sensors that have response times shorter than the sampling rate. The standards recommendations for temperature measurement are previously investigated and reported in the literature (Ramin et al. 2020; Ramin et al. 2020; Ramin et al. 2021). According to these studies, the requirements for accurate sensible effectiveness measurements depend on FBR configurations and design conditions (NTU, Cr^*, and λ). Furthermore, it was concluded that temperature sensor requirements in these standards are rigorous and could be relaxed depending on the test configurations and operating conditions. Properties measurement requirements for combined heat and moisture transfer in the desiccant-coated FBRs, however, have not been studied in the literature and this paper examines these measurement requirements.

Overall, in this paper, a transient numerical model is presented and validated for heat and moisture transfer in desiccant-coated FBRs and sensors. The model is then used to provide insights into the complex process of heat and moisture transfer in FBRs and humidity sensor measurements and provide guidance for the test standards when measuring the transient outlet properties of desiccant-coated FBRs.

2 FBR configurations and outlet property profiles

The outlet property profiles of air streams (temperature and humidity) depend on the FBRs configurations and location of sensors. According to the number of exchangers, there are two FBRs configurations, namely single-core and double-core FBRs. Generally, it can be concluded that the measurement sensors are exposed to either a positive/negative sawtooth or semi-sawtooth profile depending on the configuration of FBRs. The sawtooth profile consists of positive or negative (depends on the direction of energy transfer from the airstream to the exchanger or from the exchanger to the airstream) ramps, while the semi-sawtooth profile has a horizontal part before a positive or negative ramp. This flattened part (horizontal part) of the semi-sawtooth profile

represents the initial condition of measurement sensors before the sensors are exposed to the FBR outlet airstream. In other words, the sensors in FBRs with semi-sawtooth profiles are exposed to the inlet conditions followed by the outlet conditions, while sensors in FBRs with sawtooth profiles are always exposed to the outlet conditions.

Table 1 presents FBR configurations in literature and the test standards along with their outlet air property profiles (sawtooth or semi-sawtooth profile). According to Table 1, the sensors at the outlet of double-core exchangers in the CSA C439-18 standard (CSA Group 2018) and ASHRAE standard 84 (ASHRAE 2019) experience a periodic positive sawtooth profile for a hot and humid period and a periodic negative sawtooth profile for a cold and dry period. Also, for the double-core exchanger developed by Tempeff (Tempeff North America 2020), the supply side sensors are exposed to a sawtooth profile while those on the exhaust side experience semi-sawtooth profile. For the single-core exchanger or room-based energy recovery exchanger (ventilator) (Borodulin and Nizovtsev 2018), as shown in Table 1, the sensors at the FBR supply and exhaust sides are exposed to a semi-sawtooth profile that is labeled exchanger sensor in Table 1.

A small-scale test facility was developed by Krishnan et al. (Krishnan et al. 2020) at the University of Saskatchewan to evaluate the performance of FBRs; a schematic of the test section in the small-scale test facility is presented in Table 1. The exchanger in the test section is moved between two airflow ducts to replicate the alternating nature of FBRs. To measure air properties at the outlet of the exchanger, a set of measurement sensors are attached to the exchangers (called exchanger sensors that move with the exchanger), and another set is fixed to the airflow ducts (called duct sensors), as shown in the Table. The duct and exchanger sensors are exposed to different airstream profiles as they have different initial conditions, but both are exposed to semi-sawtooth profile.

Table 1. Different configurations of FBRs and their corresponding outlet air property profiles (temperature and humidity)

#	**Sawtooth properties profile**		**Semi-sawtooth properties profile**	
	Hot & humid outlet	Cold & dry outlet	Hot & humid outlet	Cold & dry outlet
Profile shape	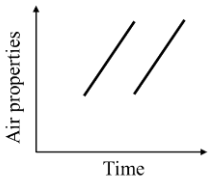	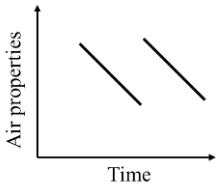	(a) Exchanger sensor 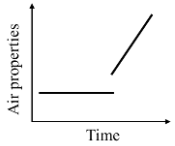	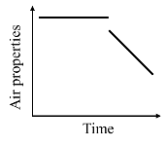
			(b) Duct sensor 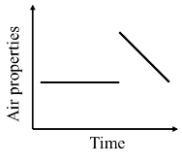	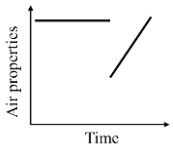
	Examples in literature		Examples in literature	
	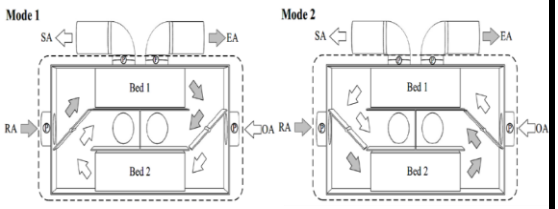 Ref: ASHRAE standard 84 (ASHRAE 2019)		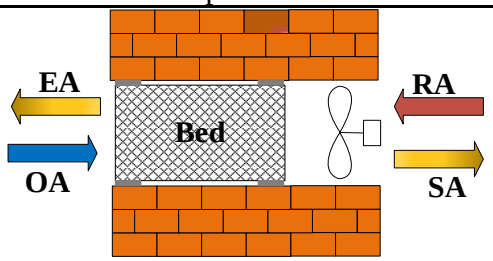 Ref: Room-based ventilation (Nizovtsev et al. 2016)	
	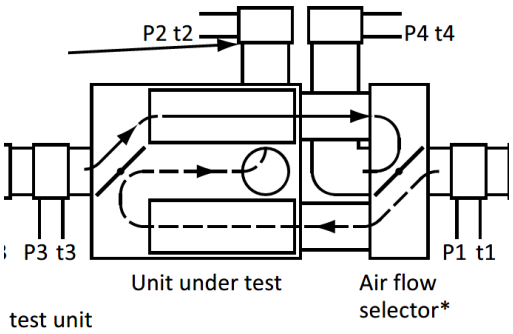 Ref: CSA C439-18 standard (CSA Group 2018)		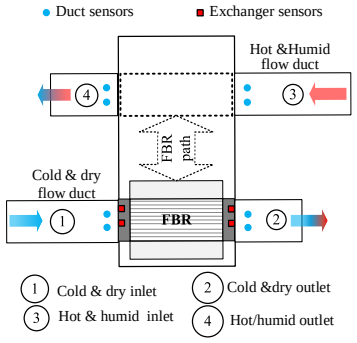 Ref: Small-scale test facility (Krishnan et al. 2020)	
	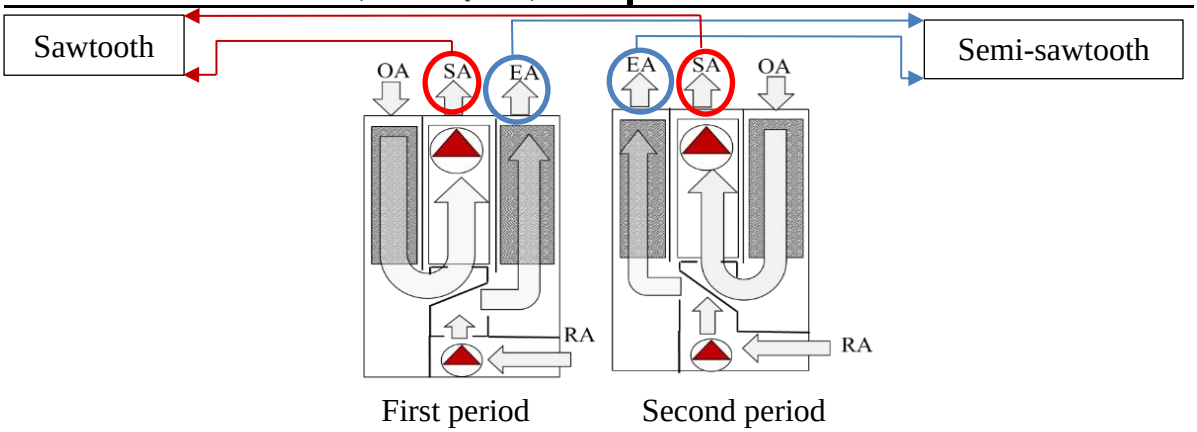 Ref: Double-core FBRs manufactured by Tempeff (Tempeff North America 2020)			

From the above discussions and Table 1, it can be concluded that three sensor configurations can be considered for desiccant-coated FBRs: (1) sensors exposed to sawtooth profile, (2) exchanger sensors, and (3) duct sensors. The latter two sensors are exposed to semi-sawtooth profiles.

3 Performance parameters

The performance of an FBR is quantified using effectiveness (CSA Group 2018; ASHRAE 2019), and the sensible, latent (or moisture), and total (or enthalpy) effectiveness are represented by Eqns. (1), (2), and (3) respectively for both the hot and humid and cold and dry periods.

Sensible effectiveness	$\varepsilon_{sh} = \frac{\dot{m}_{hh} Cp_g \left(\overline{T}_{hh,o} - T_{hh,i}\right)}{\min(C_{hh}, C_{cd}) \left(T_{hh,i} - T_{cd,i}\right)}$ $\varepsilon_{sc} = \frac{\dot{m}_{cd} Cp_g \left(\overline{T}_{cd,o} - T_{cd,i}\right)}{\min(C_{hh}, C_{cd}) \left(T_{hh,i} - T_{cd,i}\right)}$	(1)
Latent effectiveness	$\varepsilon_{lh} = \frac{\dot{m}_{hh} \left(W_{hh,i} - \overline{W}_{hh,o}\right)}{\min(\dot{m}_{hh}, \dot{m}_{cd}) \left(W_{hh,i} - W_{cd,i}\right)}$ $\varepsilon_{lc} = \frac{\dot{m}_{hh} \left(\overline{W}_{cd,o} - W_{cd,i}\right)}{\min(\dot{m}_{hh}, \dot{m}_{cd}) \left(W_{hh,i} - W_{cd,i}\right)}$	(2)
Total effectiveness	$\varepsilon_{th} = \frac{\dot{m}_{hh} \left(H_{hh,i} - \overline{H}_{hh,o}\right)}{\min(\dot{m}_{hh}, \dot{m}_{cd}) \left(H_{hh,i} - H_{cd,i}\right)}$ $\varepsilon_{tc} = \frac{\dot{m}_{hh} \left(\overline{H}_{cd,o} - H_{cd,i}\right)}{\min(\dot{m}_{hh}, \dot{m}_{cd}) \left(H_{hh,i} - H_{cd,i}\right)}$	(3)

The symbols in the above equation are defined in the nomenclature. The temperature, humidity, and enthalpy of the air at the outlet of FBR vary with time; hence the time-averaged values (Temperature: $\overline{T}_{cd,o}$ and $\overline{T}_{hh,o}$, humidity: $\overline{W}_{cd,o}$ and $\overline{W}_{hh,o}$, and enthalpy: $\overline{H}_{cd,o}$ and $\overline{H}_{hh,o}$), are used in the effectiveness evaluation in the above equations. The time-averaged outlet air prosperities for any variable (χ : temperature, humidity, or enthalpy) in the cold and dry period (Eqn. (4)) and the hot and humid period (Eqn. (5)) are calculated as follows.

$$\bar{\chi}_{\mathrm{cd,o}} = \frac{1}{\mathrm{P_{cd}}} \int_0^{\mathrm{P_{cd}}} \chi_{\mathrm{cd,o}} \mathrm{dt}, \quad (4)$$

$$\bar{\chi}_{\mathrm{hh,o}} = \frac{1}{\mathrm{P_{hh}}} \int_0^{\mathrm{P_{hh}}} \chi_{\mathrm{hh,o}} \mathrm{dt}, \quad (5)$$

P_{cd} and P_{hh} are the duration of the hot (and humid) and cold (and dry) periods, respectively. The enthalpy of air is calculated in Eqn. (6).

$$H = Cp_g T + W(h_{fg} + Cp_w T), \quad (6)$$

4 Numerical model for exchanger (FBR) and measurement sensors

Instantaneous temperature and humidity ratio profiles at the outlet of a desiccant-coated FBR during both hot (and humid) and cold (and dry) periods are required to quantify errors due to the transient response of temperature and humidity sensors. In this paper, a mathematical model developed by Simonson and Besant (Simonson and Besant 1997a; 1997b) is used to obtain the instantaneous temperature and humidity profile which is called FBR model. The FBR model provides the actual outlet condition from the FBR without including the impact of sensors. Then models for the temperature and humidity sensors (sensor model) are implemented to capture what would be measured using sensors. The combined FBR and sensors model results can be compared with experimental measurements as the measurements from an experiment include sensor responses. The FBR model, temperature sensor model, and humidity sensor model are presented in the following subsections.

4.1 FBR model

In FBR, the two separate air streams (hot (and humid) stream and cold (and dry) stream) alternately flow through the energy exchanger, which consists of numerous channels. Because of the similarity between the flow channels, the governing equations will be presented for a single channel. The schematic of the cross-section of an airflow channel is shown in Figure 2. In the hot

and humid period, the energy from the hot and humid airstream is absorbed (solid lines in Fig. 2) in the matrix, which is then transferred to the cold and dry air during the subsequent cold and dry period (dashed line in Fig. 2).

The 1-D (bulk mean temperature and moisture concentration) governing equations presented by Simonson and Besant (Simonson and Besant 1999b; 1999a) for desiccant-coated regenerators are adopted in this paper. The conservation of mass in the air stream results in two continuity equations (7 and 8), for water vapor and dry air as follows:

$$A_g \frac{\partial \rho_v}{\partial t} + \frac{\partial}{\partial x}\left(\rho_v v A_g\right) + \dot{m}' = 0 \quad (7)$$

$$\frac{\partial \rho_a}{\partial t} + \frac{\partial}{\partial x}\left(\rho_a v\right) = 0 \quad (8)$$

Where v is the mean airflow velocity, $\dot{m}'$ is the rate of phase change per unit of exchanger length, A_g is the cross-sectional area of the channel, ρ_v is water vapor density and ρ_a is dry air density.

The conservation of mass for the desiccant is as follows:

$$\dot{m}' = \rho_{d,dry} A_d \frac{\partial u}{\partial t} \quad (9)$$

Where $\rho_{(d,dry)}$ is the density of dry desiccant, and A_d and u are the surface area of the desiccant, and mass fraction of water in the desiccant, respectively. The energy conservation equations for coupled heat and moisture transfer in the airstream (Eqn. (10)) and exchanger matrix (Eqn. (11)) are as follows:

$$\rho_g C_{P_g} A_g \frac{\partial T_g}{\partial t} + U \rho_g C_{P_g} A_g \frac{\partial T_g}{\partial x} - \dot{m}' h_{ad} \eta + h \frac{A_s'}{L}\left(T_g - T_m\right) = 0 \quad (10)$$

$$\rho_m C_{P_m} A_m \frac{\partial T_m}{\partial t} - \dot{m}' h_{ad}(1-\eta) - h \frac{A_s'}{L}\left(T_g - T_m\right) = \frac{\partial}{\partial x}\left(k_m A_m \frac{\partial T_m}{\partial x}\right) \quad (11)$$

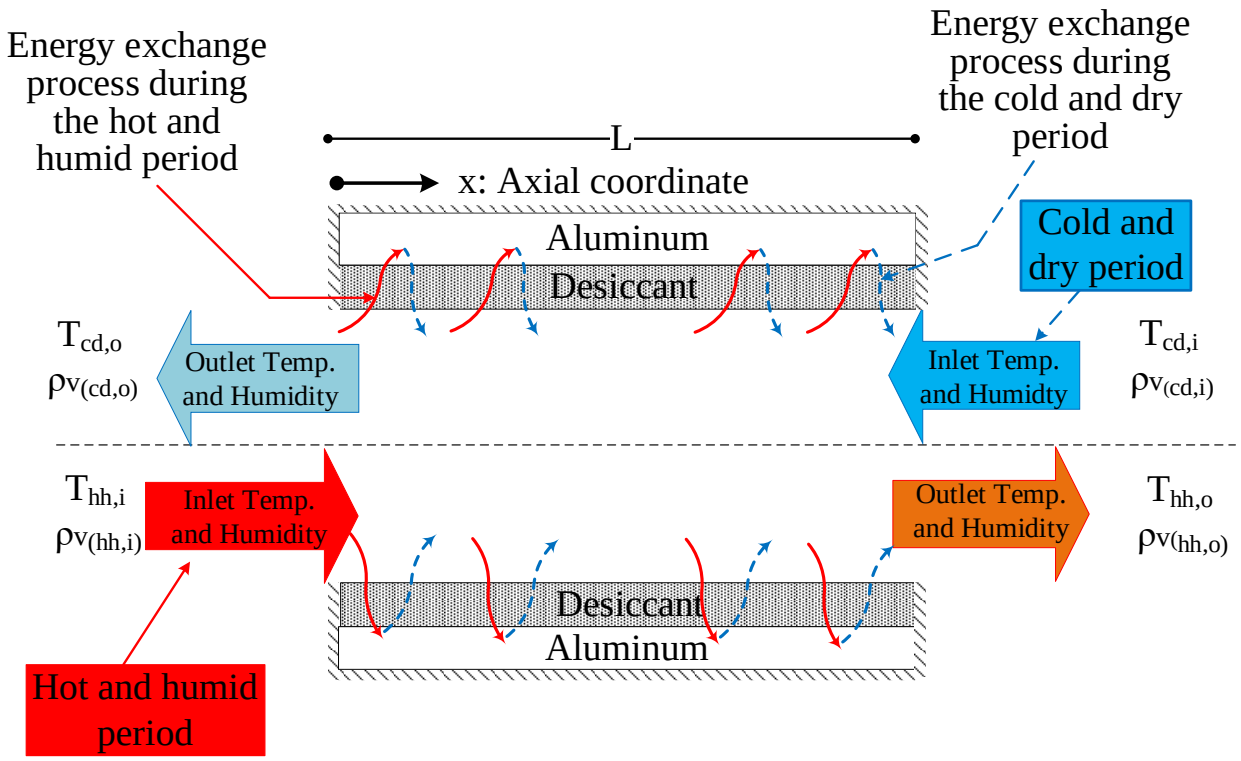

Figure 2. A schematic of the numerical domain for heat and mass transfer in a representative channel of desiccant-coated FBR

Where t, x, C_p, k, h, L, and T are time, axial coordinate, specific heat, thermal conductivity, convective heat transfer coefficient, length of the channel, and temperature, respectively. Subscripts 'g' and 'm' are used to represent the air and matrix (desiccant + aluminum) variables, respectively. A'_s and A_m represent heat transfer surface area and cross-sectional area of the exchanger plate. The term η in the above equations represents the distribution of phase change energy between the desiccant and the airflow (Simonson and Besant 1999b; 1999a). η is determined form Eqn. (12).

$$\eta = \frac{k_g/\sqrt{\alpha_g}}{k_g/\sqrt{\alpha_g} + k_m/\sqrt{\alpha_m}} \qquad (12)$$

α_g and α_m are thermal diffusivity of the airflow and matrix, respectively and $k_g = hD_h$. The value of η is expected to be between 0 and 0.1 (Simonson and Besant 1999a). Several thermodynamics

correlations are required to complete the formulation of the problem; these equations could be found in (Simonson 1998).

Moisture transfer between the air stream and the desiccant during adsorption and desorption is obtained from Eq. (13):

$$\dot{m}' = h_m \frac{A_s'}{L} (u_v - u_{v,m}) \quad (13)$$

Where h_m and $u_{v,m}$ are the convective mass transfer coefficient and mass fraction of water vapor on the surface of desiccant, respectively. The convective mass transfer coefficient, h_m, is determined using the analogy between heat and mass transfer assuming Lewis number is unity and $u_{v,m}$is obtained from the sorption isotherms.

The inlet conditions during the hot (and humid) and cold (and dry) periods are presented in Eqns. (14)-(17).

$$T_g(x = 0, nP \le t \le nP + P_{hh}) = T_{hh,i}\ ; \qquad n = 0,1,2, \ldots \quad (14)$$

$$T_g(x = L, nP + P_{hh} \le t \le (n+1)P) = T_{cd,i}\ ; \qquad n = 0,1,2, \ldots \quad (15)$$

$$\rho_v(x = 0, nP \le t \le nP + P_h) = \rho_{v_{hh,i}}(t); \qquad n = 0,1,2, \ldots \quad (16)$$

$$\rho_v(x = 0, nP + P_{hh} \le t \le (n+1)P) = \rho_{v_{cd,i}}(t); \quad n = 0,1,2, \ldots \quad (17)$$

In the above equations, the integer n is used to have alternate inlet conditions (hot (and humid) and cold (and dry)) in FBR. The inlet conditions could be a function of time but constant values are considered in this study. Furthermore, heat and mass transfer at the ends of the channel are considered to be negligible and thus the boundary conditions can be written as:

$$\left.\frac{\partial T_m}{\partial x}\right|_{x=0} = \left.\frac{\partial T_m}{\partial x}\right|_{x=L} = 0 \quad (18)$$

$$\left.\frac{\partial u}{\partial x}\right|_{x=0} = \left.\frac{\partial u}{\partial x}\right|_{x=L} = 0 \tag{19}$$

The fundamental dimensionless groups for heat and mass transfer in desiccant-coated regenerators have been derived from the governing equations presented in Eqns. (7,8, 10, 11) (Simonson and Besant 1999; Simonson and Besant 1999a). Simonson and Besant (1999a) derived the fundamental dimensionless groups for heat and moisture transfer for desiccant-coated regenerators. These equations are presented as follows.

$$\frac{\partial \rho_v}{\partial \mathrm{x}^*} = \mathrm{NTU_{mt}}\left(\rho_{\mathrm{v,m}} - \rho_{\mathrm{v}}\right) \tag{20}$$

$$\frac{\partial \rho_{\mathrm{v,m}}}{\partial \mathrm{t}^*} = \frac{\mathrm{NTU_{mt}}}{Cr^*_{mt}}\left(\rho_{\mathrm{v}} - \rho_{\mathrm{v,m}}\right) \tag{21}$$

$$\frac{\partial \mathrm{T}^*_{\mathrm{g}}}{\partial \mathrm{x}^*} = \mathrm{NTU_{ht}}\left(\mathrm{T}^*_{\mathrm{m}} - \mathrm{T}^*_{\mathrm{g}}\right) \tag{22}$$

$$\frac{\partial \mathrm{T}^*_{\mathrm{m}}}{\mathrm{Cr}^*_{\mathrm{ht}}} = \frac{\mathrm{NTU_{ht}}}{Cr^*_{ht}}\left(\mathrm{T}^*_{\mathrm{g}} - \mathrm{T}^*_{\mathrm{m}}\right) \tag{23}$$

Where $\mathrm{NTU_{mt}}$ is the number of moisture transfer units, Cr^*_{mt} is the matrix moisture capacity ratio, $\mathrm{NTU_{ht}}$ is the number of heat transfer units and Cr^*_{ht} is the matrix heat capacity ratio of the desiccant-coated exchanger. These variables are given in Eqns. (24) to (27).

$$\mathrm{NTU_{mt}} = NTU_o = \left(\frac{1}{\dot{m}Cp_g}\right)_{min}\left[\frac{1}{(hA_s)_{hh}} + \frac{1}{(hA_s)_{cd}}\right]^{-1} \tag{24}$$

$$Cr^*_{mt} = Crm^* \frac{\partial u}{\partial RH}\left(\frac{e^{\frac{5294}{T_{ave}}}}{10^6} - 1.61\mathrm{RH_{ave}}\right) \tag{25}$$

$$NTU_{ht} = \frac{NTU_o}{1 + \eta\frac{\epsilon_l}{\epsilon_s}H^*} \tag{26}$$

$$Cr^*_{ht} = \frac{Cr^*}{1 + \eta\frac{\epsilon_l}{\epsilon_s}H^*} \tag{27}$$

Where NTU_o and $Cr^* = \frac{\mathrm{MC_{p,m}/P}}{\dot{m}\mathrm{c_{P,g}}}$ are the overall number of heat transfer units and the matrix heat capacity rate ratio for the sensible regenerators. ϵ_l and ϵ_s are the latent and sensible effectiveness and H^* is the operating condition factor (Simonson and Besant 1999). Unlike the

dimensionless groups for sensible regenerators (Ramin et al. 2021), the dimensionless groups for heat and moisture transfer (Eqns. (24)-(27)) are functions of the operating conditions (temperature and humidity) (Simonson and Besant 1999).

$H^*$is the ratio of latent to sensible energy differences of air streams at the inlets of the FBR.

$$\mathrm{H}^* = \frac{\Delta H_l}{\Delta H_s} \tag{28}$$

Figure 3 shows lines of H^* on the psychrometric chart for the supply conditions of 23℃ and 50% of RH. The operation condition factor lies between +6 and -6 for many practical conditions in HVAC application (Simonson and Besant 1999a). $H^* = \infty$ represents the isothermal condition where both airstreams have the same inlet temperatures but different humidity ratios (i.e., $\Delta T_{inlet}=0$, $\Delta W_{inlet}\neq 0$). On the other hand, at the non-isothermal conditions, the inlet temperature and humidity on the supply and exhaust sides of FBR are not equal (i.e., $\Delta T_{inlet}\neq 0$, $\Delta W_{inlet}\neq 0$ except for $H^* = 0$ where the humidity ratios of the inlet airflows are equal while the temperatures of airstreams are different (i.e., $\Delta T_{inlet}\neq 0$, $\Delta W_{inlet}=0$)).

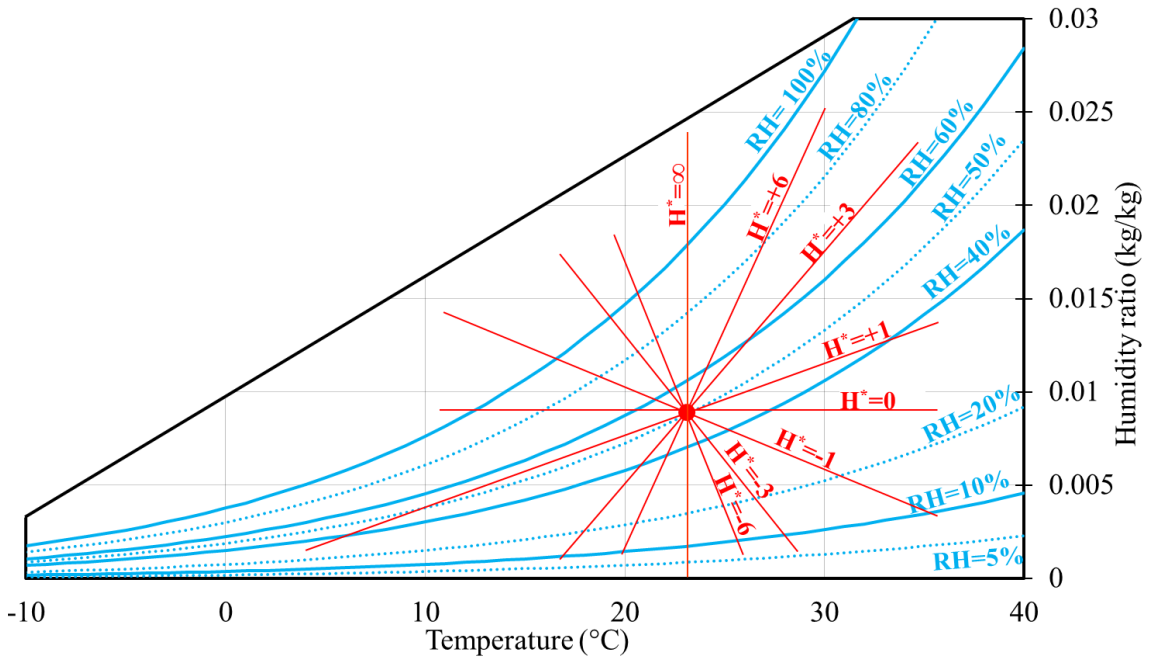

Figure 3. Lines of H^* on the psychrometric chart for supply condition of 23°C and 50% RH

For many practical applications, P_{hh} and P_{cd} are equal, and hence, they are considered to be equal in this paper as well. Also, the flow in regenerators are considered to be balanced ($C^* = \frac{C_{cd}}{C_{hh}} = 1$), as it is in the test standards (CSA C439-18 standard (CSA Group 2018) and ASHRAE standard 84 (ASHRAE 2019)), and hence the results of the present study are presented for such a balanced flow condition.

4.2 Temperature sensor model

The temperature sensor model for the temperature sensors, (Bergman L. et al. 2011; Ramin, Krishnan, Annadurai, et al. 2021) is presented in Eqn. (29).

$$\frac{dT_s}{dt} = \frac{1}{\tau_s}\left(T_g - T_s\right) \tag{29}$$

where τ_s is the time constant of the temperature sensor, and T_s is the temperature that is measured by the temperature sensor and T_g is the actual air temperature that the sensor is exposed to it.

4.3 Humidity sensor model-capacitive relative humidity sensor model

A capacitive relative humidity sensor (CRHS) correlates the electrical capacity of the sensor with RH at a reference temperature and corrects it for other temperatures. Thus, the transient response of a CRHS must be carefully analyzed for measurements in the environment, such as the outlet of FBRs where there are simultaneous changes in humidity and temperature. Experimental measurements in the literature show that CRHS might show anomalous measurements when there are humidity and temperature changes concurrently (Kaplya, Kaplya, and Silaev 2020). Kaplya et al. (2020) presented a mathematical model for the CRHS humidity measurement process to explain this anomaly. Their model assumes that CRHS is an integrated microprocessor system that performs joint processing of humidity ratio and temperature (using an internal temperature sensor). Therefore, the humidity ratio is assumed to be measured first. The microprocessor element of CRHS converts the humidity ratio to relative humidity using the environment temperature measured by the internal temperature sensor of the CRHS. This process, along with the actual measurement process of CRHS, is presented in Table 2. There are two sensor delays corresponding to the humidity ratio measurement and the internal temperature sensor of the CRHS (in step 2 at Table 2) and an additional delay (in step 4 at Table 2) for the separate temperature sensor to convert the measured RH to humidity ratio for effectiveness calculations. The proposed procedure for CRHS is presented in Eqns. (30) to (33). Once RH is obtained from this model, humidity ratio is to be calculated for effectiveness evaluations (Eqn.(32)). Thus, using RH from CRHS model and T_s from the temperature sensor model, humidity ratio is obtained (Eqn. (33)).

$$\frac{dW_{int}}{dt} = \frac{1}{\tau_{h,int}}\left(W_g - W_{int}\right) \tag{30}$$

$$\frac{dT_{int}}{dt} = \frac{1}{\tau_{t,int}}\left(T_g - T_{int}\right) \tag{31}$$

$$RH_s = f_1(W_{int}, T_{int}) \tag{32}$$

$$W_s = f_2(RH_s, T_s) \quad (33)$$

Subscript "int" represents the internally calculated values. The variables $\tau_{h,int}$ and $\tau_{t,int}$ are the internal humidity time constant and the internal temperature time constant of the humidity sensor, respectively. Also, T_s is obtained from the temperature sensor model (from Eqn. (29)) and W_s is the humidity ratio that is measured by the humidity sensor.

Table 2. Comparison of the procedure for RH measurement between the actual procedure and proposed procedure in this paper

Actual RH measurement process	**Proposed procedure to model measurement of RH**
1. Change of dielectric constant of hygroscopic dielectric material 2. The dielectric material electrical capacity changes with RH that is correlated to RH of the environment that the sensor is located.	1. Humidity ratio and temperature (actual values) are obtained from the numerical model (W_g and T_g) 2. Actual humidity ratio and temperatures will be delayed based on the time constants obtained for the CRHS (W_{int} and T_{int}). 3. Relative humidity (RH_s) is obtained with (W_{int} and T_{int}) from step 2. 4. With RH_s from step 3 and temperature from the temperature sensor model (T_s), the sensor humidity ratio (W_s) is obtained.
Note: Time constants are usually obtained at isothermal conditions(Vaisala 2019; Wang et al. 2006).	**Note:** Three delays are involved in this approach. Two delays correspond to the temperature and humidity ratio in step 2. An additional delay for temperature also exists when RH is converted to humidity ratio at step 4.

To obtain the internal time constants for humidity and temperature for the current humidity sensor model ($\tau_{h,int}$ and $\tau_{t,int}$), two experiments are designed. (1) the CRHS is exposed to a positive/negative step change in humidity ratio at a constant temperature to obtain the internal humidity ratio's time constant ($\tau_{h,int}$) and (2) the CRHS is exposed a positive/negative step change in temperature at a constant humidity ratio to estimate the internal temperature sensor's time constant ($\tau_{t,int}$).

Figure 4 shows the results for the negative and positive step changes in humidity ratio while the temperature is kept constant (Experiment (1)). The sensor in the test section (which is explained in the experimental section) is used to measure the time constants. In the experiments in Fig. 4, the inlet relative humidity was changed by 30%, and the temperature is maintained at 23°C. The experimental data were fitted to an exponential function using the trust region optimization algorithm in MATLAB 2019b (Mathworks-Inc. 2019). The exponential function for positive and negative step change is shown in Eqn. (34).

$$f(t) = \begin{cases} 1 - e^{-\frac{t}{\tau}} & positive\ step\ change \\ e^{-\frac{t}{\tau}} & negative\ step\ change \end{cases} \quad (34)$$

The time constants for positive and negative step changes in humidity ratio at constant temperature ($\tau_{h,int}$) are calculated to be 6.3 and 6.2 seconds, respectively. The average value of negative and positive step changes ($\tau_{h,int}$=6.25s) will be used for validation of the results in section 6.

Figure 5 shows the relative humidity measurement and the fitted model (from Eqn. (34)) for the second experiment with a step change in temperature while the humidity ratio is kept constant (T_{cold}=23°C and T_{hot}=38°C). Following the same approach for the humidity ratio step change experiment, the CRHS internal temperature time constants ($\tau_{t,int}$) were calculated to be 28 and 25 seconds for the negative and positive step changes in temperature, respectively. The average value of negative and positive step changes for the experiment ($\tau_{t,int}$=26.5s) will be used for validation of the results in section 6.

In order to compare the model prediction with the actual humidity sensor response, two experiments were conducted where the sensor was exposed to a step change in humidity ratio at a constant RH, and the results are compared with the humidity sensor model prediction in Fig. 6 (a)

and (b). The average time constants from positive and negative step changes experiments from Figs. 4 and 5 (i.e., a time constant of 6.25 seconds for $\tau_{h,int}$ and time constant of 26.5 seconds for $\tau_{t,int}$), are used in the model in Fig. 6. Also, the temperature sensor time constant of 1.5s (τ_s=1.5s, as presented in Table 3) is used for the comparison in Fig. 6.

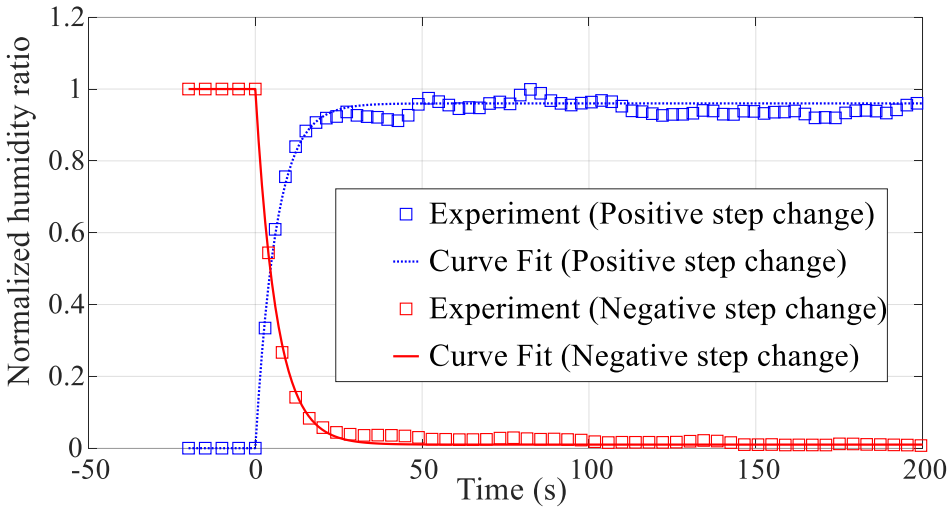

Figure 4. Negative and positive step changes in humidity ratio at constant temperature (T=23 °C) to obtain the internal humidity ratio's time constant ($\tau_{h,int}$)

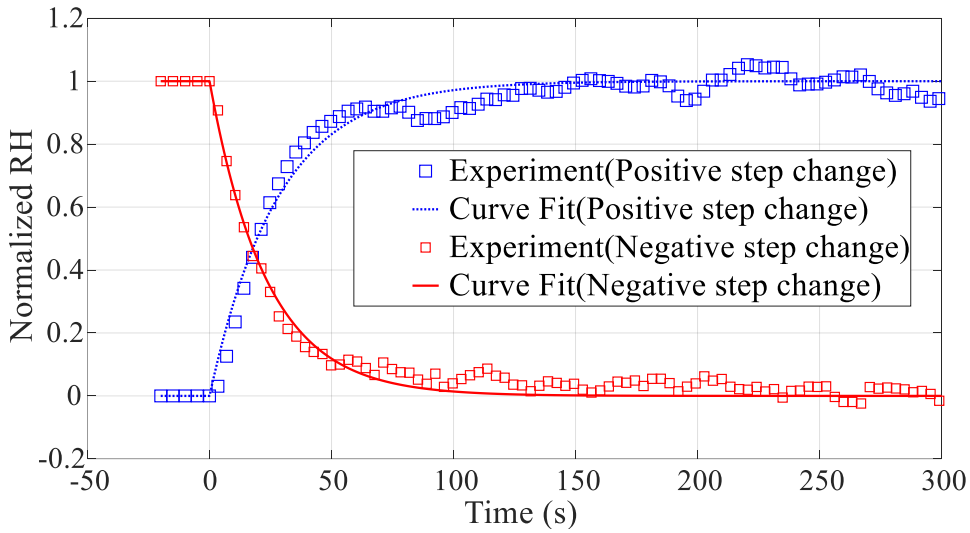

Figure 5. Negative and positive step change in temperature and measured RH with CRHS at constant humidity ratio to obtain the internal temperature time's constant ($\tau_{t,int}$)

A good agreement between the results from the experiments and the humidity sensor model is observed in Fig. 6. More specifically, an overshoot in the humidity ratio can be seen at the

beginning of both negative and positive step changes in Figs. 6, and the model also predicts this overshoot which is not theoretically possible. This unexpected response at non-isothermal conditions can be attributed to the change in dielectric constant due to the simultaneous changes in humidity and temperature. Similar behaviour for capacitive humidity sensors has been reported previously in the literature (Kaplya, Kaplya, and Silaev 2020).

(a). A negative step change in humidity ratio at a constant RH

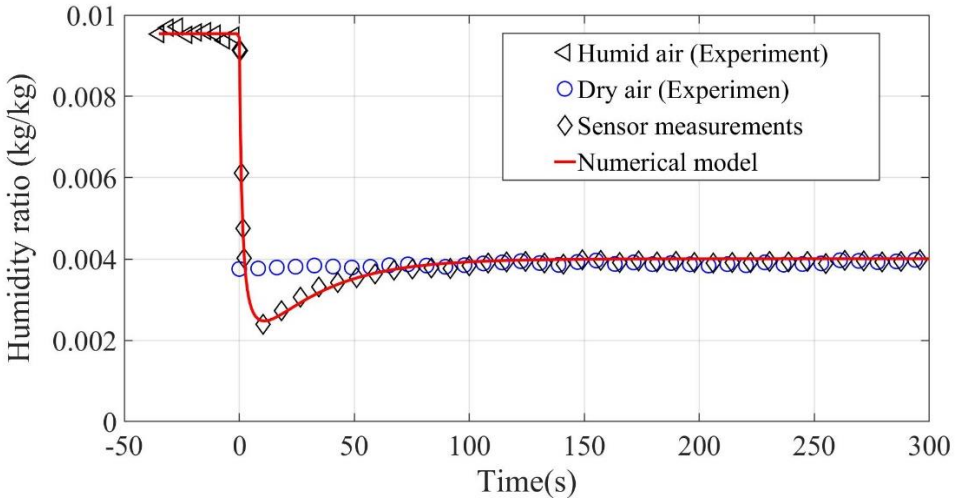

(b). A positive step change in humidity ratio at a constant RH

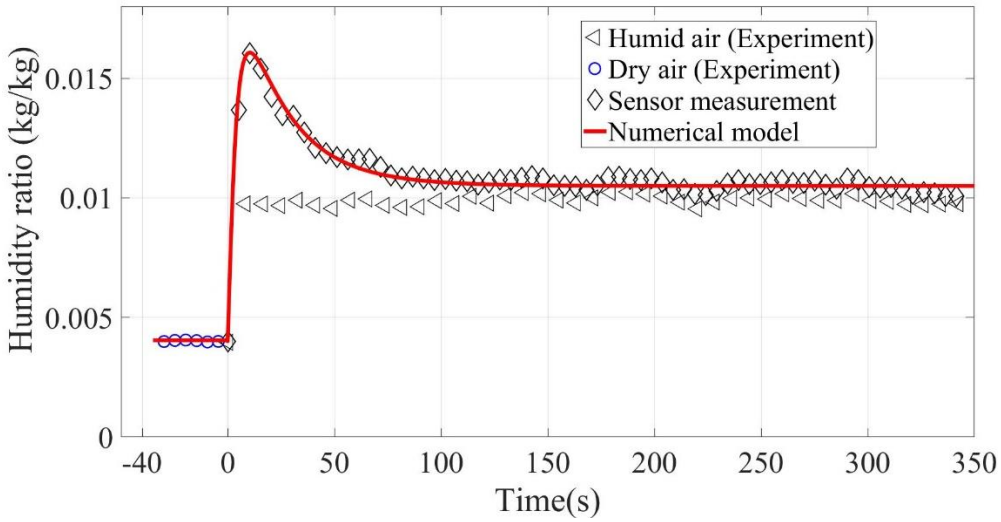

Figure 6. Comparison of experiment and humidity sensor model for a negative and positive step change in humidity ratio at a constant RH

4.4 Numerical solution procedure

The governing conservation energy and mass equations are discretized using a finite volume method (Versteeg and Malalasekera 2007). The upwind differencing and central differencing schemes are used to approximate the convection and diffusion terms in the airflow and the matrix (Aluminum + desiccant), respectively (Versteeg and Malalasekera 2007). The resulting algebraic equation for the airflow is solved using Gauss-Seidel iteration technique, and the Tridiagonal Matrix Algorithm (TDMA) is used to solve the energy equation in the matrix (Versteeg and Malalasekera 2007). A MATLAB code is developed to solve the set of algebraic equations. A flowchart for the numerical solution procedure is presented in Fig. 7.

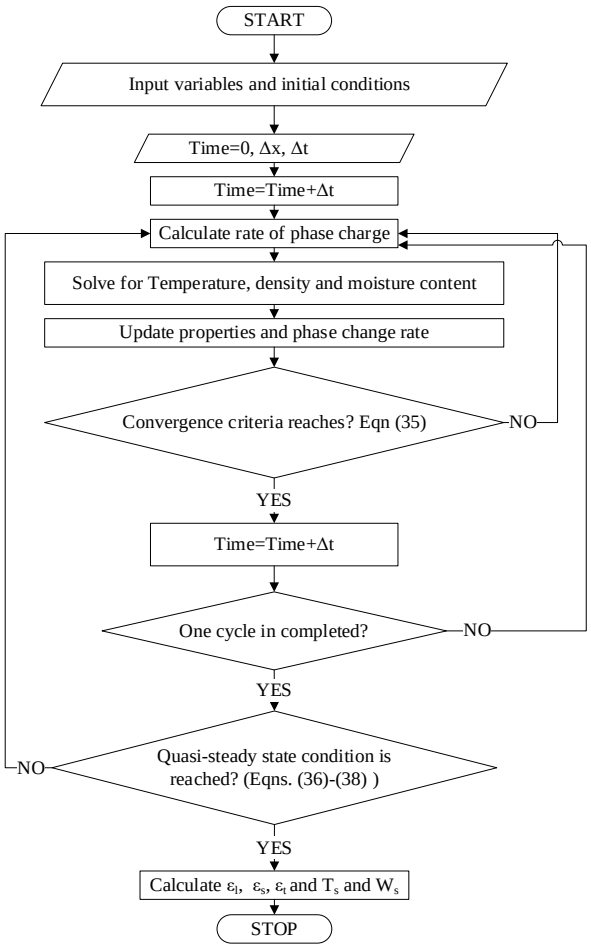

Figure 7. Numerical procedure flowchart

The solution starts with an initial condition and time is incremented when the convergence criteria (Eq. (35)) for each dependent variables (temperature, and humidity) and the rate of phase change are satisfied.

$$\frac{\sum_{i=1}^{N_s}\left|\chi(i)^{j+1}-\chi(i)^{j}\right|}{n(\chi_{max}-\chi_{min})} \leq 10^{-5} \tag{35}$$

When the convergence criterion is reduced to 10^{-6}, a negligible (less than 0.05%) impact was found on the predicted effectiveness. Upon completion of each complete cycle (one hot and humid period + one cold and dry period), the quasi-steady-state conditions in Eqns. (36)-(38) are examined.

$$\left|\frac{\dot{m}_h\left(H_{h,i}-H_{h,o}\right)-\dot{m}_c\left(H_{c,o}-H_{c,i}\right)}{\min(\dot{m}_h,\dot{m}_c)\,(H_{h,i}-H_{c,i})}\right| \leq 10^{-2} \tag{36}$$

$$\left|\frac{\dot{m}_h\left(W_{h,i}-W_{h,o}\right)-\dot{m}_c\left(W_{c,o}-W_{c,i}\right)}{\min(\dot{m}_h,\dot{m}_c)\,(W_{h,i}-W_{c,i})}\right| \leq 10^{-2} \tag{37}$$

$$\left|\frac{\partial \epsilon}{\partial t}\right| \approx \left|\frac{\epsilon^{k}-\epsilon^{k-1}}{P}\right| \leq 10^{-4} \tag{38}$$

Eqns. (36) and (37) ensure that the energy and moisture balance between the energy stored in the first period and energy released in the subsequent period. Eqn. (38) compares the effectiveness values from each completed cycle to the previous cycle before reaching the quasi-steady-state condition. If the solutions satisfy the quasi-steady-state conditions (Eqns(36)-(38)), the numerical procedure is completed; otherwise, time is further incremented until the solution reaches a quasi-steady-state condition.

The numerical solution is performed on a uniform 1-D grid with a constant time step. The grid dependency tests are performed to determine the optimum spatial grid size and time step. Further details on the numerical solution procedure could be found in the literature (Simonson and Besant 1997a; 1997b; Ramin et al. 2021).

The FBR model gives accurate outlet air properties (without the impacts of sensors), which is used to calculate the correct effectiveness values. The temperature and humidity ratio from the FBR model are used as inputs for the temperature and humidity sensor models. Subsequently, the sensor models predict the measured T_s and W_s by the sensors in an experiment.

5 FBR small-scale test facility

A schematic of the small-scale test facility is shown in Fig. 8. The desiccant-coated exchanger (EX in Fig. 8) is moved alternately between two conditioned airstreams. A schematic of the exchanger is shown in Fig. 9. When the exchanger is exposed to hot and humid air, the desiccant adsorbs the moisture, and the matrix (aluminum) stores the heat (hot and humid period). The heat and moisture stored in the exchanger are then transferred to the cold and dry airstream during the subsequent exposure of the exchanger to a cold and dry airstream (cold and dry period). The experiment is continued until the exchanger attains a quasi-steady-state condition.

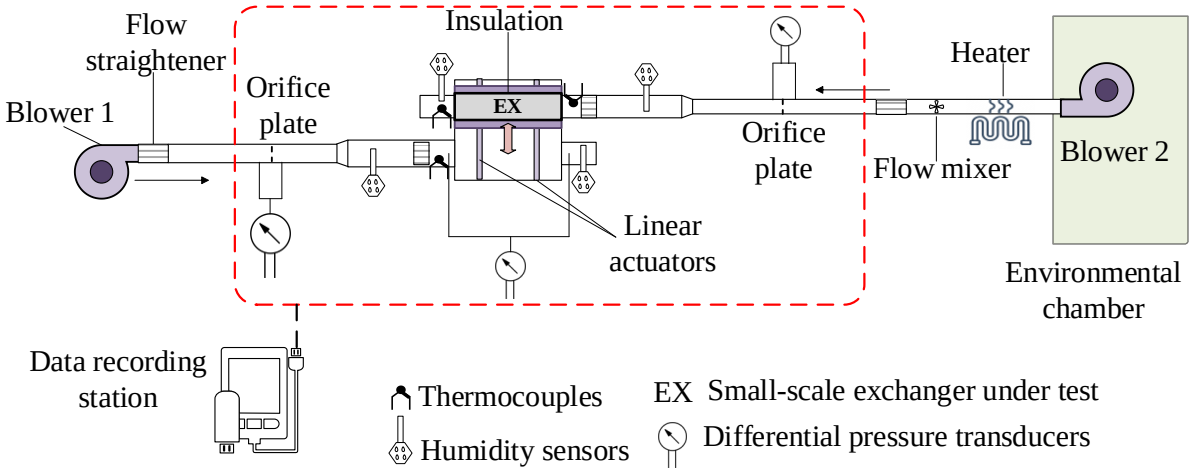

Figure 8. Schematic of the small-scale test facility (Krishnan et al. 2020)

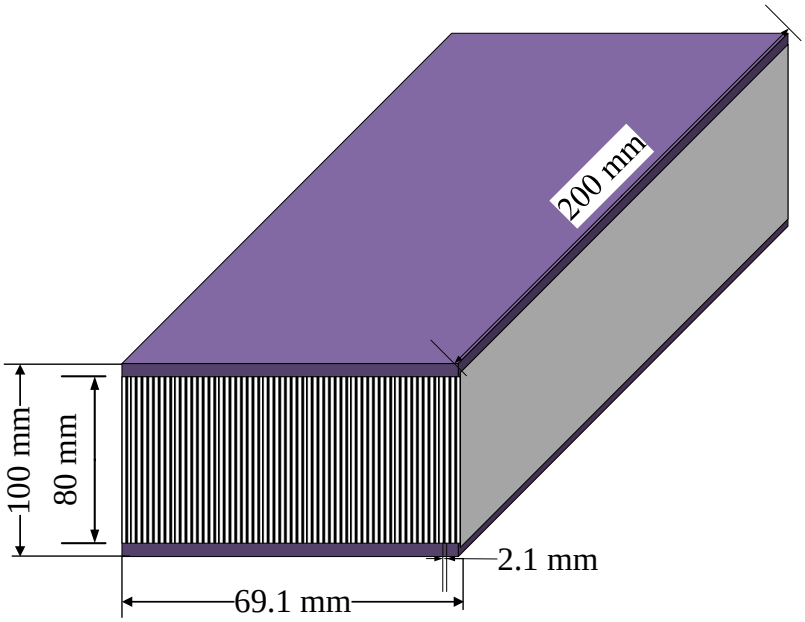

Figure 9. A schematic of the small-scale exchanger (Krishnan et al. 2020)

The temperatures of the airstreams are measured using calibrated T-type thermocouples with an uncertainty of ±0.2 °C. Capacitive humidity sensors with an uncertainty of ±1.5% (percentage points) are used to measure the humidity of the airstreams. Orifice plates with differential pressure transducers with a total uncertainty of ±8 Pa are also used to measure flow rates. The uncertainty in flow rate measurements is calculated to be ±2%.

The small-scale exchanger consists of 26 equally spaced desiccant-coated aluminum plates. The geometric details, thermo-physical properties of the exchanger, and the time constants of sensors are presented in Table 3. A uniform monolayer silica gel desiccant is coated on both sides of the aluminum plates using the sieving method developed at the University of Saskatchewan (Krishnan et al. 2022). The physical properties of desiccants and details of desiccant coating are reported in Table 3. Experiments on silica gel were conducted using the Gravimetric Analyzer system (IGA-002, manufacturer: Hiden Isochema Ltd., United Kingdom) to obtain the silica gel sorption isotherm curve shown in Fig.10. Sorption isotherm curve is used to predict the

adsorption-desorption characteristics of the desiccant as a function of relative humidity. The adsorption curve is used in the validation of the numerical model in section 6. More details about sorption isotherm experiments and desiccant-coated exchangers can be found in (Krishnan et al. 2022). Krishnan et al. (2020; 2019) has documented the principle of operation, instrumentation, and data analysis procedures of the experiments.

Uncertainty analysis has been performed by following the rule of error propagation to maintain a 95% confidence interval (Figliola and Beasley 2010), and the uncertainties in the sensible effectiveness and latent effectiveness are ±3% and ±7%, respectively. Energy balance tests were performed, and results showed that the test facility conserves energy within ±5% for a wide range of test conditions.

Table 3. Geometrical details, thermophysical properties of the exchanger, dimensionless parameters, and sensor time constant

Exchanger channel	Length(mm)	200
	Width (mm)	80
	Height (mm)	2.1
	Hydraulic diameter (mm)	4.1
Aluminum plates	Thickness (mm)	0.69
	Thermal conductivity (W/m·K)	2730
	Density (kg/m^3)	220
	Specific heat capacity (J/kg·K)	904
Silica gel properties	Density (kg/m^3)	350
	Specific heat capacity (J/kg·K)	333
	Mass of coating (g)	45.4
	Desiccant/matrix mass ratio (%)	4.8
Temperature Sensor	Time constant (s)	1.5
Humidity sensor	Temperature time constant- $\tau_{t,int}$ (s)	26.5
	Humidity ratio time constant- $\tau_{h,int}$ (s)	6.25

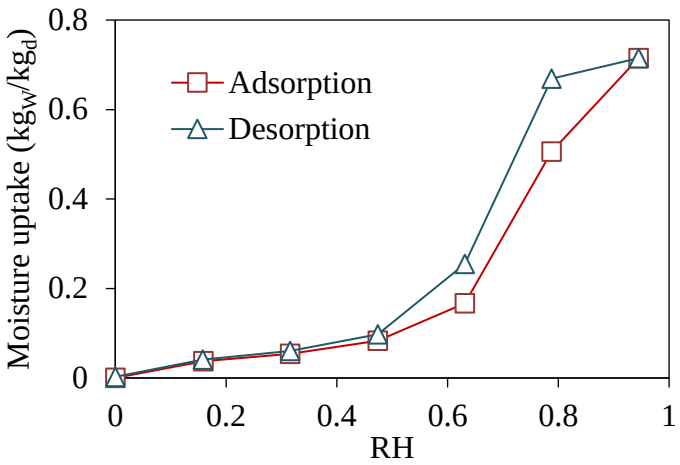

Figure 10. Sorption isotherm of silica gel at 25 °C

5.1 Bag sampling method

Bag sampling method (BSM) is proposed by ASHRAE 84 (ASHRAE 2019) and CSA C 439-18 (CSA Group 2018) standards as an alternative to humidity sensors for accurate measurement of the average humidity ratio (and hence latent effectiveness) at the outlet of FBRs over a period. A sample of FBR outlet air is collected in a bag during the entire period then the bag is allowed to reach equilibrium with the environment (the sampling is repeated several times to compare the samples). The average humidity ratio and hence the latent effectiveness is obtained by measuring the relative humidity and temperature of the air in the bag. The experimental setup, instrumentation, and sampling procedure for the BSM are explained in detail in the literature (ASHRAE 2019; CSA Group 2018). The BSM uncertainty is ±7% in effectiveness.

6 Validation of results

In this section, the numerical model will be validated against experimental results from the small-scale test facility. The experimental (which includes the sensor responses) temperature and humidity ratio profiles for both isothermal and non-isothermal conditions will be compared against the combined FBR and sensor models. The effectiveness results from the FBR model will also be

compared with experimental results from the bag sampling method (BSM) as this method does not contain the transient response of sensors. Moreover, the current model results have been previously compared and validated with experimental measurements available in the literature for isothermal conditions (Ramin, Krishnan, and Simonson 2020).

6.1 Validation under isothermal conditions ($H^* = \infty$ or $\Delta T_{inlet}=0$, $\Delta W_{inlet}\neq 0$)

Figure 11 compares the quasi-steady state humidity ratio profile from the experiment, the FBR model, and the combined FBR and sensor model for the exchanger sensor (Fig. 11 (a)) and the duct sensor (Fig. 11 (b)) at operating conditions in Table 4. The combined FBR and sensor model results agree with the experiment measurement for both exchanger and duct sensors. The difference between the FBR model (which neglects the sensor transients) and the experimental results are the greatest at the beginning of each period as expected. The difference is especially prevalent for the duct sensors which are exposed to the largest step change in conditions before periods. By the end of each period, the FBR models and experimental data show a good agreement.

Table 4. Inlet conditions for the isothermal experiment ($\Delta T_{inlet}=0$, $\Delta W_{inlet}\neq 0$)

Hot and humid air		Cold and dry air		Recovery	Face velocity	H^*
Temp. (°C)	RH (%)	Temp. (°C)	RH (%)	period (s)	(m/s)	
28	61	28	37	60	1.5	∞

Table 5 compares the latent effectiveness values from the FBR model, combined FBR and sensor model, and the experiment for the isothermal test conditions. The FBR model provides the correct effectiveness value, while the other values are affected by the sensor transients, as mentioned in the model development section. The comparison in this table shows that the combined FBR and sensor model prediction of latent effectiveness agrees with the experimental measurements within ±2% which verifies the combined FBR and sensor model. The exchanger

sensors overpredict and the duct sensors underpredict the latent effectiveness for the isothermal condition ($\mathbf{H^* = \infty}$).

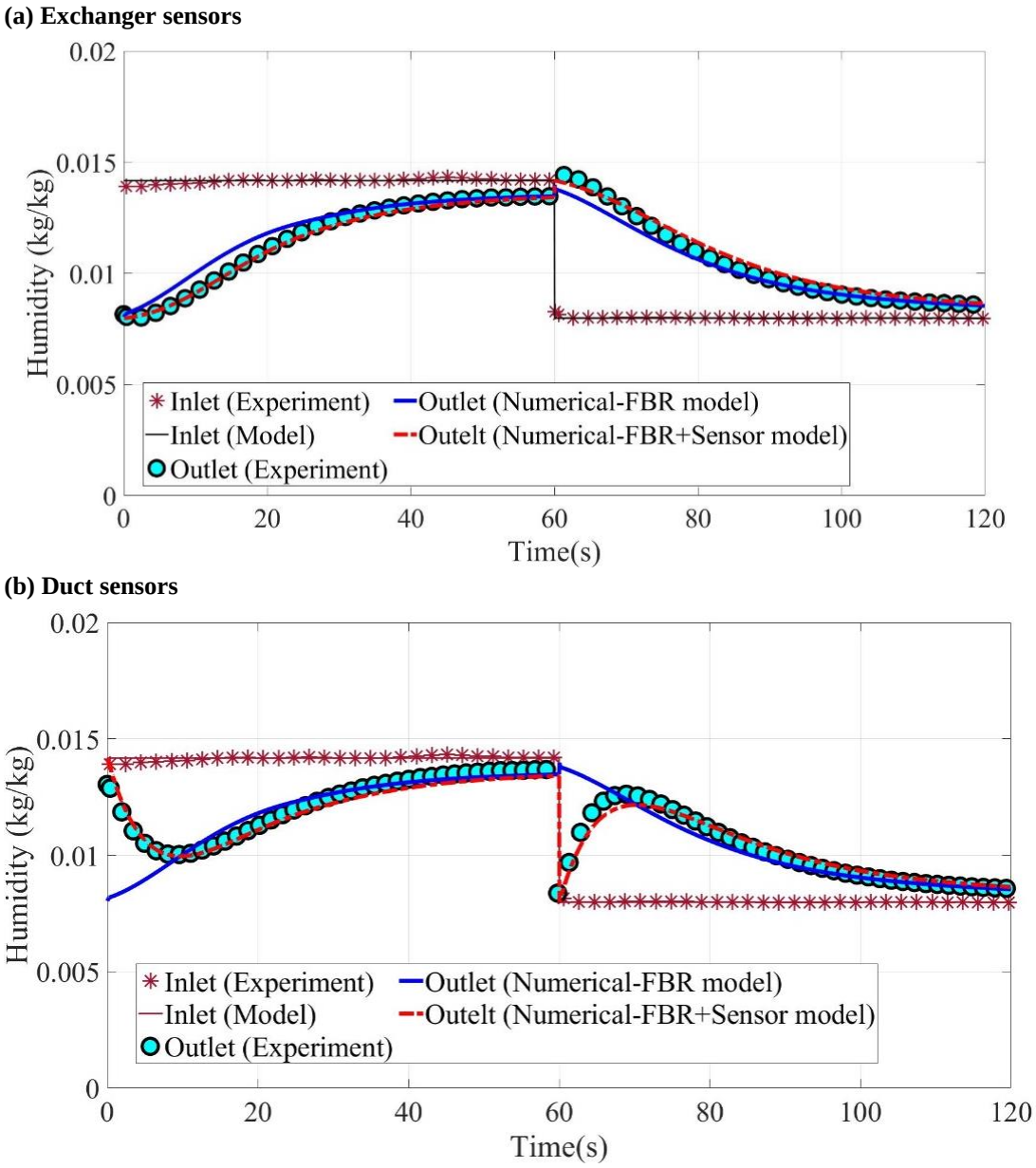

Figure 11. Comparison of outlet humidity ratio profile for (a) exchanger and (b) duct sensor between experiment and numerical models (FBR model and FBR+ Sensor model)

Table 5. Comparison of latent effectiveness from the experiment, FBR model, and the combined FBR and sensor model for the isotherm test conditions (or $\Delta T_{inlet}=0$, $\Delta W_{inlet}\neq 0$)

FBR model	FBR+ sensor	Experiment	FBR+ sensor	Experiment
	Exchanger sensor-hot and humid side		Exchanger sensor-cold and dry side	
36.0%	41.3%	43±7 %	37.3%	38±7%
	Duct sensor-hot and humid side		Duct sensor-cold and dry side	
36.0%	31.0%	33±7 %	28.2%	30±7%

6.2 Validation under non-isothermal conditions ($H^* = 0.85$ or $\Delta T_{inlet}\neq 0$, $\Delta W_{inlet}\neq 0$)

The experimental and models (the FBR model and the combined FBR and sensor model) temperature and humidity profiles at the quasi-steady state condition are compared for the exchanger and duct sensors in Figs. 12 and 13, respectively. The inlet conditions for this non-isothermal experiment are presented in Table 6. The model predictions for the temperature profile from both the exchanger and duct sensors are in good agreement with the experimental measurements. It should be noted that during the cold period, the duct sensors on the hot duct are exposed to the ambient lab conditions (T=23°C and RH=50%), and hence, the temperature and humidity ratio values do not start from the hot and humid conditions in Table 6.

An important observation is a peak in the humidity profile for the duct sensors at about 70s during the cold and dry period in Fig. 13. The measured outlet humidity ratio peaks during this period, and the value becomes higher than the inlet humid air humidity ratio, which is not theoretically possible. These experimental results are difficult to understand without the model. The combined FBR and sensor model can accurately predict this behavior, as shown in Fig. 13. Again, the FBR model provides physically realistic or correct results because it is not affected by the sensor transients. Furthermore, the humidity ratio profile for the exchanger sensor in Fig. 12 overshoots the inlet conditions at 40-60 seconds; and again the sensor model accurately predicts this phenomenon.

Table 6. Inlet conditions for non-isothermal experiment

Hot and humid air		Cold and dry air		Recovery	Face velocity	H^*
Temp. (°C)	RH (%)	Temp. (°C)	RH (%)	period (s)	(m/s)	
38.3	18.5	14.8	23.2	60	1.5	0.85

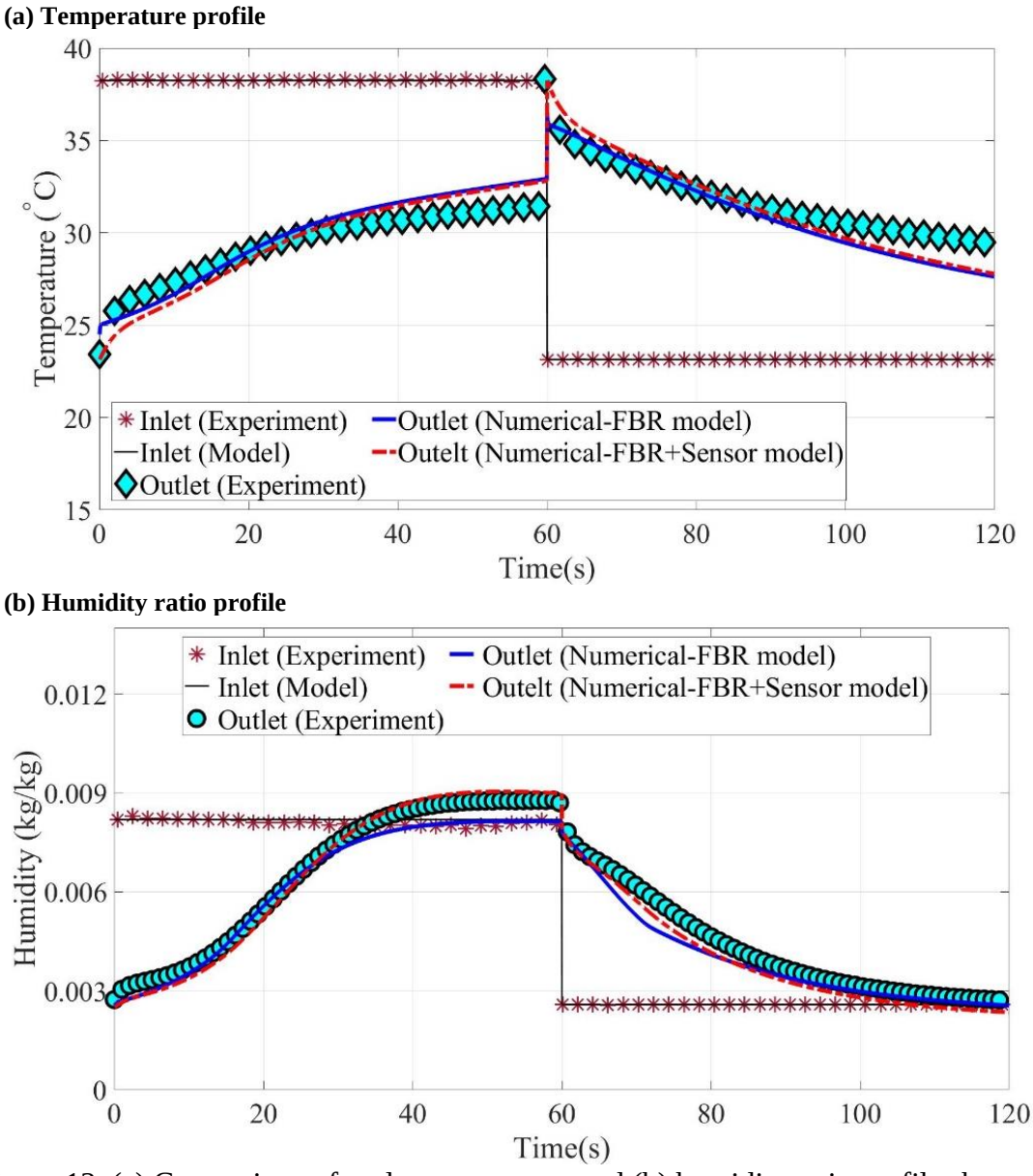

Figure 12. (a) Comparison of outlet temperature and (b) humidity ratio profiles between experiment, numerical model (FBR model), and combined FBR and sensor model for the exchanger sensors

Table 7 compares the latent and sensible effectiveness values from the FBR model, combined FBR and sensor model, and the experiment for the non-isothermal experiment. Comparing the results shows that the combined FBR and sensor model results agree with the experimental measurements within ±2% and ±1% for latent and sensible effectiveness which validate the model. The duct sensor on the dry and cold period predicts the latent effectiveness of about 20% higher than its actual value, mainly because of the peak in humidity caused by the transient response of the humidity sensor.

Table 7. Comparison of latent effectiveness from experiment, FBR model, and combined FBR and sensor model

Latent effectiveness				
FBR model	**FBR+ sensor**	**Experiment**	**FBR+ sensor**	**Experiment**
	Exchanger sensor-hot and humid side		Exchanger sensor-cold and dry side	
26.0%	18.5%	21±7%	27.0%	29±7%
	Duct sensor-hot and humid side		Duct sensor-cold and dry side	
26.0%	32.5%	31±7%	44.2%	46±7%
Sensible effectiveness				
FBR model	**FBR+ sensor**	**Experiment**	**FBR+ sensor**	**Experiment**
	Exchanger sensor-hot side		Exchanger sensor-cold side	
55.6%	57.7%	58±3%	56.3	57±3%
	Duct sensor-hot side		Duct sensor-cold side	
55.6%	58.0%	57±3%	54.6	55±3%

(a) Temperature profile

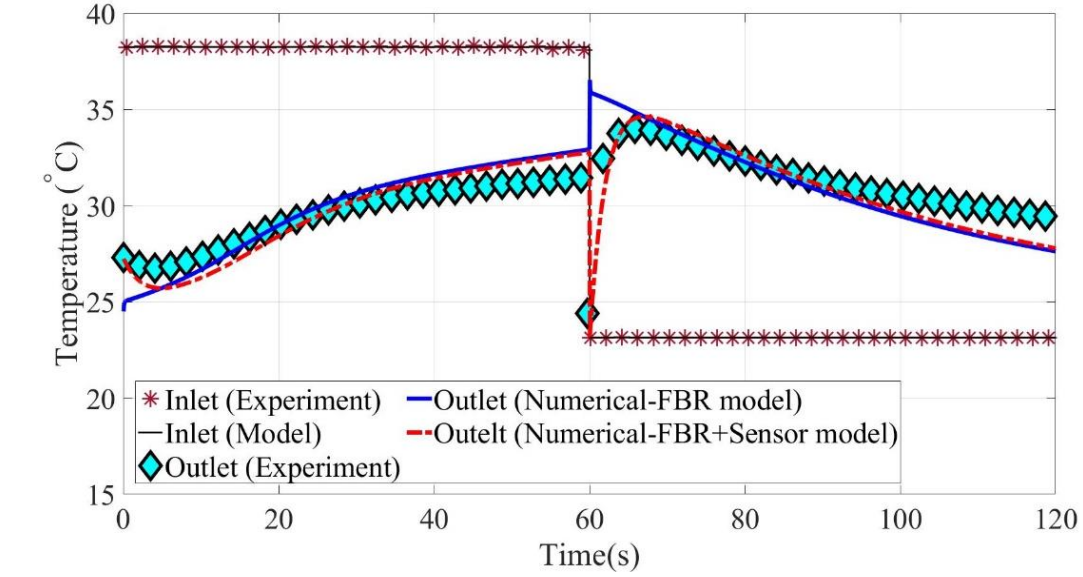

(b) Humidity ratio profile

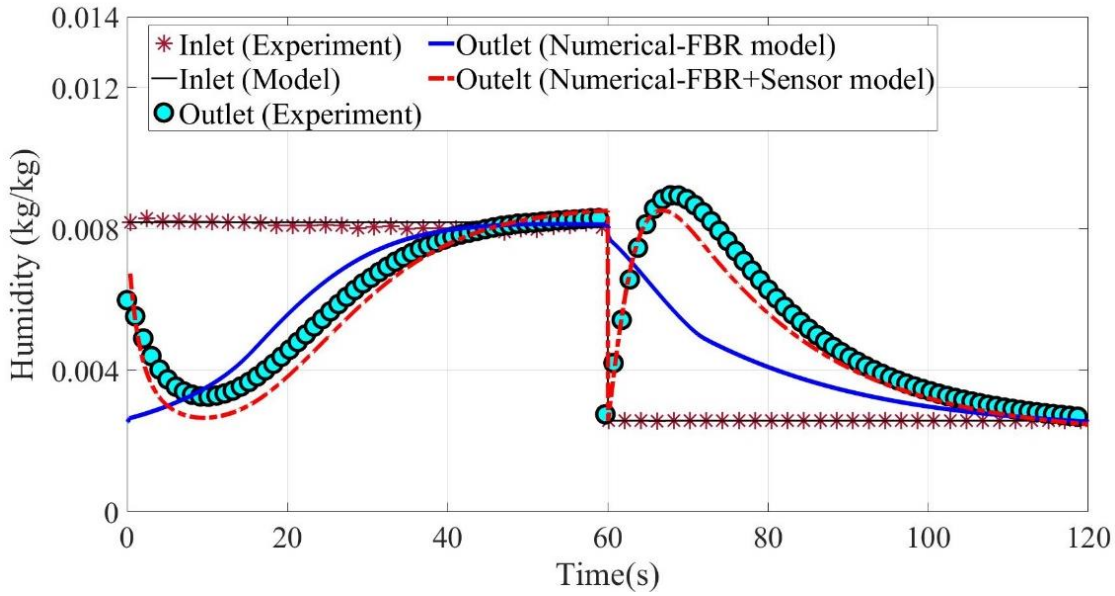

Figure 13. (a) Comparison of outlet temperature and (b) humidity ratio profiles between experiment, numerical model (FBR model), and combined FBR and sensor model for the duct sensors

6.3 Effectiveness comparison for the FBR model

Latent effectiveness from the numerical model (FBR model) is compared against the results obtained from the bag sampling method (BSM); the results are presented in Fig. 14 for different test conditions (face velocity: 1-2 m/s, NTU_o: 1.8 – 3) at both isothermal and non-

isothermal conditions. The numerical results agree with the BSM within the experimental uncertainty limits. Furthermore, a recently published experimental paper from our group documented a comprehensive comparison of the numerical model prediction, BSM method, and the experimental results (measured with sensors) for a wide range of operating and design conditions (E. N. Krishnan et al. 2022). The findings from this paper indicate a good agreement between the model and experimental measurements from both BSM and sensors.

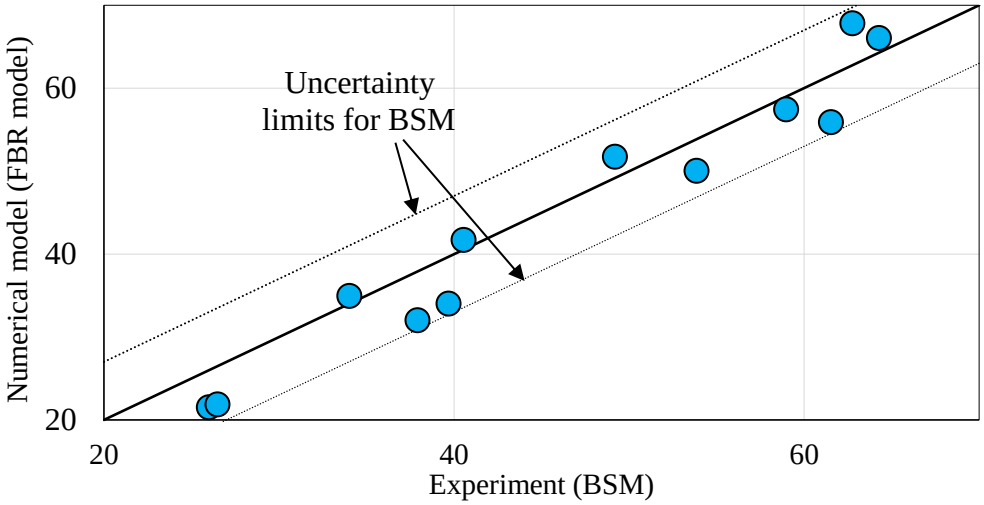

Figure 14. Comparison of latent effectiveness from the numerical model (FBR) and BSM at several non-isothermal conditions (face velocity: 1-2 m/s, NTU_o: 1.8 – 3)

7 Applications of the combined FBR and sensor models

This section presents applications of the combined FBR and sensor model to evaluate the latent effectiveness of the desiccant-coated FBRs. The sensible effectiveness will not be presented in this section as it can be obtained from the temperature sensor measurements and the model is presented in the literature (Ramin et al. 2021; Ramin et al. 2021). The difference between effectiveness from the FBR model and the combined FBR and sensor model (FBR+ Sensor) is reported as the latent effectiveness error ($\Delta\epsilon_L$) that results due to the transient nature of FBR and temperature and humidity sensors:

$$\Delta\epsilon_L = \epsilon_{L,\mathrm{FBR}} - \epsilon_{L,FBR+sensor} \quad (39)$$

Negative $\Delta\epsilon_L$ means that the sensor transients will result in overpredicting the actual FBR effectiveness while positive error means that the sensor underpredicts the actual effectiveness.

The following sections present the quasi-steady state humidity ratio profiles of FBRs with semi-sawtooth and sawtooth outlet profiles to understand the response of the sensors when exposed to different humidity ratio profiles. Later, the latent effectiveness errors for different operating condition factors and sensor time constants are presented.

The general sorption curve (Eqn. (40)) is used in the simulation presented in this section.

$$\mathrm{u} = \frac{\mathrm{W_m}}{1 - \mathrm{C} + \mathrm{C/RH}} \quad (40)$$

In this equation $\mathrm{W_m}$ is the maximum moisture content of the desiccant, and the coefficient C is determined based on the desiccant used and u is the mass fraction of water in the desiccant. This general sorption curve can model the sorption characteristics of several desiccants such as molecular sieve, silica gel, and activated carbon (Simonson and Besant 1999b). The following simulations were performed for the linear sorption curve (C=1) with maximum moisture uptake of 0.5 (W_m=0.5). Also, the distribution of phase change energy between the desiccant and the airflow (Eqns. (10) and (11)) is chosen to be 0.1 ($\eta = 0.1$).

7.1 FBRs with a semi-sawtooth profile

Figures 15 and 16 present the quasi-steady state semi-sawtooth humidity ratio profile (FBR model) that the exchanger and duct sensors, respectively, are exposed to during a cycle time of 120 seconds in FBRs. The first half of the cycle (0-60 seconds) shows the sensor exposure to constant temperature and humidity airflow conditions (the initial condition of the sensors), and the second half of the cycle (60-120 seconds) is the FBR outlet humidity profile. The humidity ratio

profiles from the sensor (FBR+ sensor model) with time constants of ($\tau_{t,int}$=25s, $\tau_{t,int}$=5s and τ_s=3s) are also presented in these figures. The results in Figs. 15 and 16 are presented for the AHRI (Air Conditioning, Heating and Refrigeration Institute) summer test conditions (Table 8).

For the exchanger sensor in Fig. 15, the sensor measurement (FBR+ sensor model) starts from the sensor initial condition and then crosses the FBR profile during the second period (60-120s when the sensors are exposed to the outlet of FBR). The sensor measurement gradually distant from the actual values. The sensor measurement peaks during the first period (0-60 second when the sensors are exposed to inlet conditions) and then gradually become closer to the actual value by the end of the first period. Due to the simultaneous step changes in temperature and humidity, during this period (0-60s), the sensor measured values peak and then gradually become closer to the actual values.

Table 8. AHRI summer test conditions ($H^* = 1.6$)

Air properties	Supply air	Exhaust air
Dry bulb temperature	35	23.9
Wet bulb temperature	25.6	17.2

The explanation for the exchanger sensors (Fig. 15) applies to the duct sensors in Fig. 16. However, for the duct sensors (Fig.16), the sensor (FBR+ Sensor model) measures an additional peak during its exposure to the FBR outlet (about 70s) because of the simultaneous changes in temperature and humidity. But it approaches the actual values by the end of each period.

(a) cold and dry period

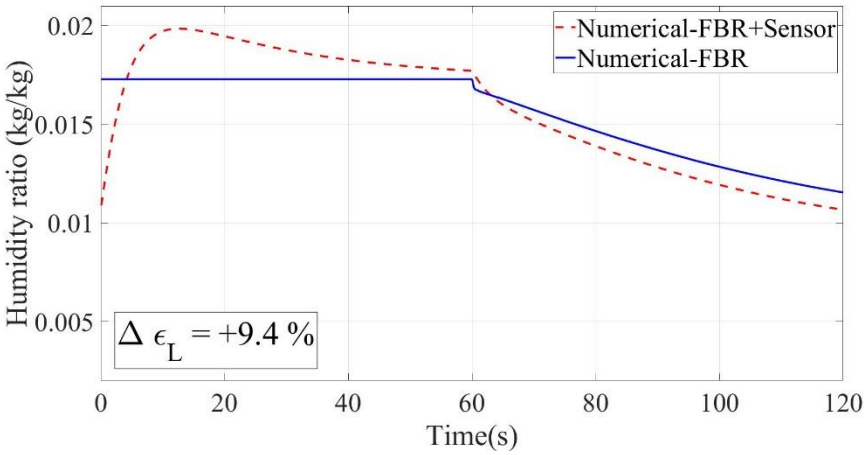

(b) hot and humid period

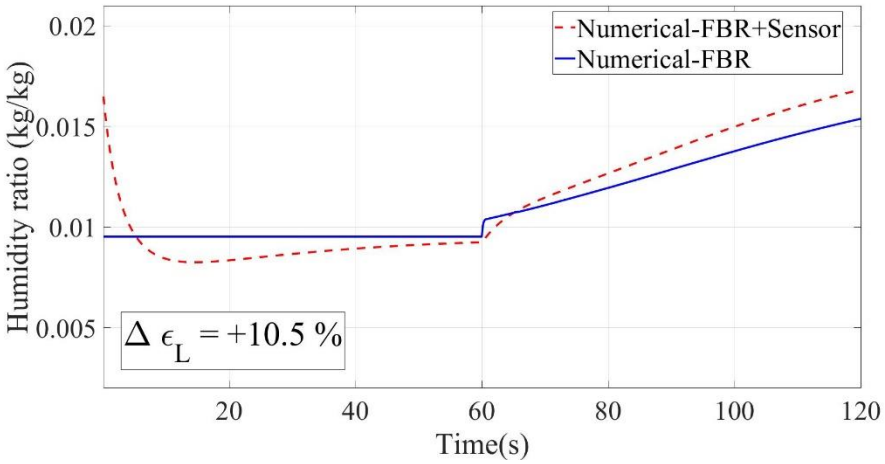

Figure 15. Quasi-steady-state humidity ratio profile (FBR model) that the exchanger sensor is exposed to and its response (FBR+ Sensor model) for time constants of $\tau_{t,int}$=25s, $\tau_{t,int}$=5s and τ_s=3s at (a) cold and dry period and (b) hot and humid period (NTU_o=3, Cr^*=3, λ=0.08, $Cr_m^* = 0.3$, $\eta = 0.1$ and at the AHRI summer test conditions ($H^* = 1.6$))

Latent effectiveness errors ($\Delta\epsilon_L$) are determined from Eqn. (39) and are also shown in Figs, 15 and 16 (cycle time of 120 seconds). The errors are significant and range from 10-20%. The exchanger sensor underestimates the latent effectiveness, while the duct sensor overestimates the latent effectiveness at this operating condition (AHRI summer test condition).

(a) cold and dry period

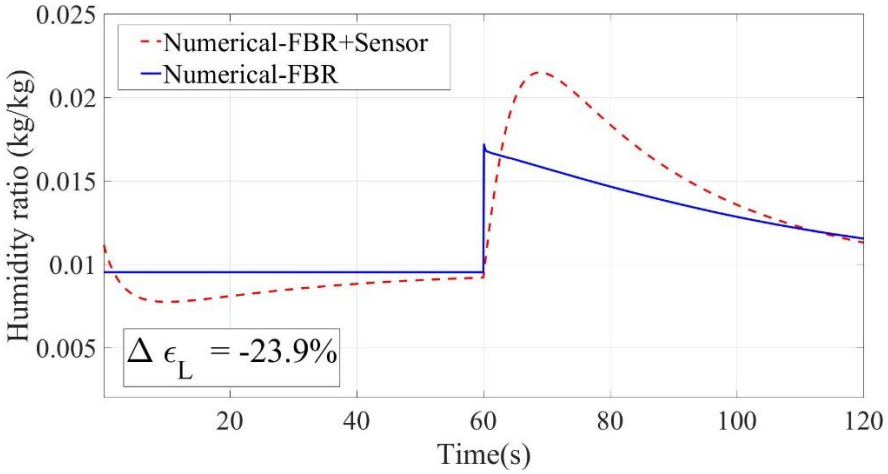

(b) hot and humid period

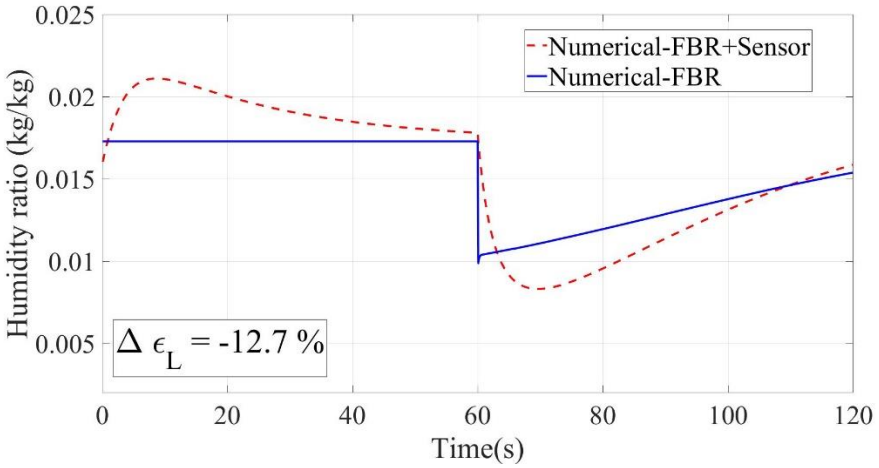

Figure 16. Quasi-steady-state humidity ratio profile (FBR model) that the duct sensor is exposed and its response (FBR+ Sensor model) for time constants of $\tau_{t,int}$=25s, $\tau_{t,int}$=5s and τ_s=3s at (a) cold and dry period and (b) hot and humid period (NTU_o=3, Cr^*=3, λ=0.08, $Cr_m^* = 0.3$, $\eta = 0.1$ and at the AHRI summer test conditions ($H^* = 1.6$))

The latent effectiveness errors on the hot (and humid) and cold (and dry) sides are not equal; this is an important observation and is different from sensible FBRs as presented in the literature (Ramin et al. 2021). For the sensible FBRs, the sensible effectiveness errors are independent of the period of operation (hot or cold) (Ramin et al. 2021), and thus averaging of effectiveness can give the accurate effectiveness of sensible FBRs. On the other hand, the latent effectiveness cannot be averaged on hot (and humid) and cold (and dry) periods to obtain the

average effectiveness, as the sensor errors (FBR+ Sensor model) depend on the period of operation.

7.2 FBRs with a sawtooth profile

Figure 17 shows the actual quasi-steady-state humidity ratio profile (FBR model) that the sensor with a sawtooth profile is exposed to along with the sensor (with time constants of $\tau_{t,int}$=25s, $\tau_{t,int}$=5s and τ_s=3s) would measure (FBR+ Sensor model) during the humid (and hot) and dry (and cold) periods. Like the previous section, two consecutive periods are presented in this figure, and both periods are the same for this type of FBR. The sensor measurement (FBR+ Sensor model) reaches a maximum value at the dry (and cold) period and gradually drops. The sensor measurement approaches a minimum value for the humid (and hot) period and gradually rises during the rest of the period. The humidity sensors underestimate the latent effectiveness for the dry (and cold) period while overestimates for the humid (and hot) period at this operating condition. The latent effectiveness error on the hot and humid period is equal to that of the cold and dry period but with an opposite sign. This is an essential practical conclusion as it can suggest that for desiccant coated FBRs exposed to a sawtooth profile, the latent effectiveness can be measured accurately by averaging the effectiveness values on the humid (and hot) and dry (and cold) periods. For sensible FBRs, the temperature sensors exposed to a sawtooth temperature profile measure the average temperatures (and thereby accurately predict the effectiveness) during each period regardless of the temperature sensor characteristics and the sides where measurements were taken (i.e., hot and cold sides of FBRs). Thus, there is no need to do averaging for sensible FBRs.

(a) cold and dry period

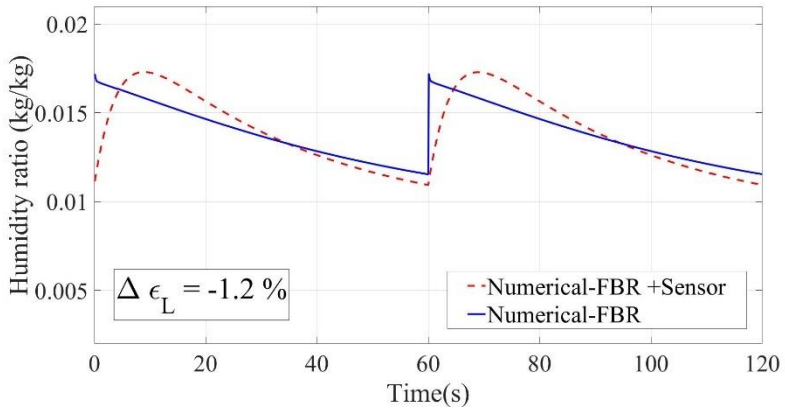

(b) hot and humid period

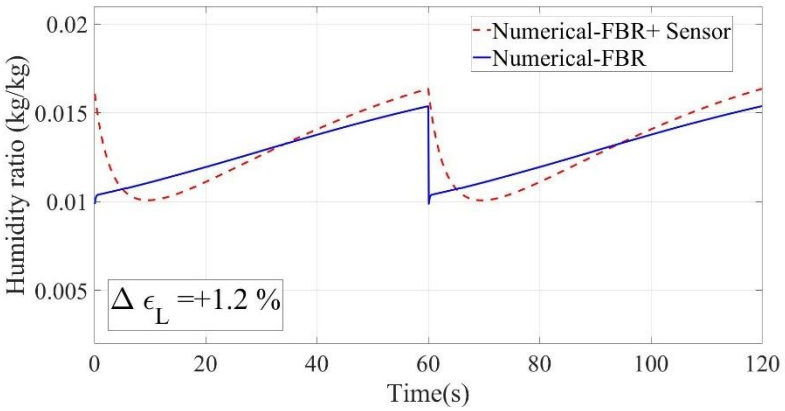

Figure 17. (a) Quasi-steady-state humidity ratio profile (FBR model) for FBR with sawtooth profile and its response (FBR+ Sensor model) for time constants of $\tau_{t,int}$=25s, $\tau_{t,int}$=5s and τ_s=3s at (a) cold and dry period and (b) hot and humid period (NTU_o=3, Cr^*=3, λ=0.08, $Cr_m^* = 0.3$, $\eta = 0.1$ and at the AHRI summer test conditions ($H^* = 1.6$))

7.3 Impact of operating condition parameter(H^*) on latent effectiveness error

The latent effectiveness error depends on the direction of heat and moisture transfer in desiccant-coated FBRs, and this could be quantified by varying H^*, the operating condition parameter factor (Fig. 3).

Figure 18 shows the latent effectiveness error while varying H^* for different sensor arrangements, i.e., duct and exchanger sensors for FBRs exposed to semi-sawtooth profiles and sensors exposed to a sawtooth profile. When H^* approaches zero (when moisture transfer is low,

but the temperature changes are high across FBR), the latent effectiveness errors increase significantly because of the large internal temperature time constant of the humidity sensor. The latent effectiveness error decreases as H^* increases which is due to the small magnitude of temperature changes in these operating conditions across the FBR.

The effectiveness errors for sensors exposed to sawtooth profiles are smaller (less than ±3% for all H^* values) than errors for sensors exposed to semi-sawtooth profiles. Furthermore, the effectiveness errors on the dry and humid sides (or supply and exhaust sides) for sensors that experience sawtooth profiles are equal but with an opposite sign, as mentioned in the previous section. Thus, the effectiveness can be average on both sides to obtain the accurate effectiveness for FBR with a sawtooth outlet profile. However, as mentioned previously, the effectiveness error on dry and humid sides of FBRs with semi-sawtooth profiles (duct and exchanger sensors) are not equal, and taking average does not cancel the effectiveness error.

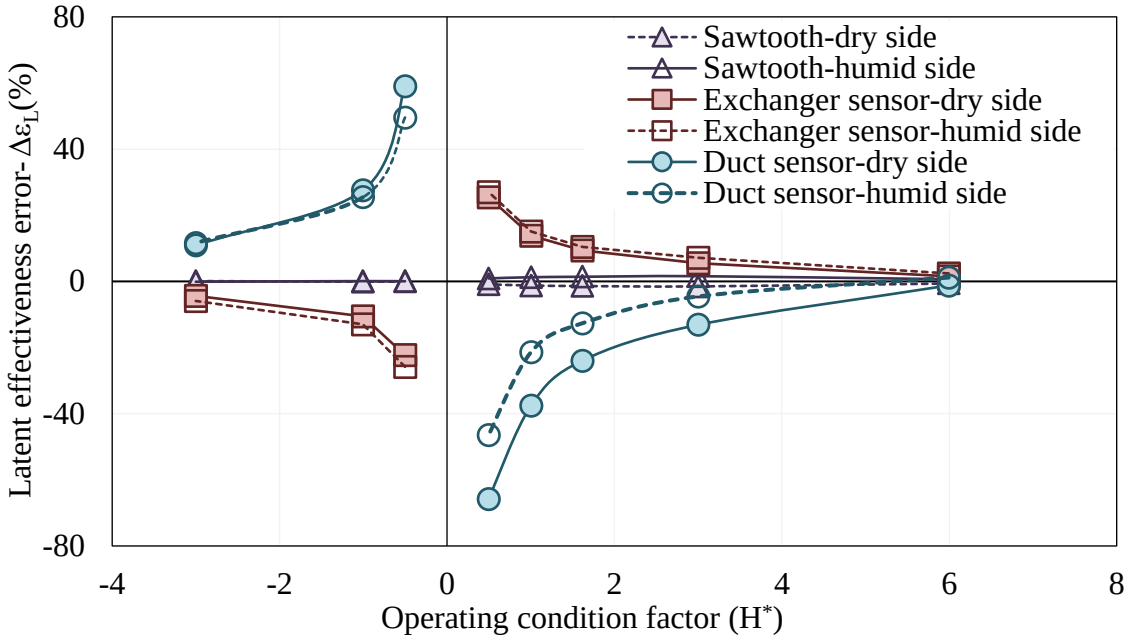

Figure 18. Effect of operating condition parameter (H*) on the latent effectiveness error at NTU_o=3, Cr^*=3, $Cr_m^* = 0.3$, and λ=0.08 and measurement sensors with time constants of $\tau_{t,int}$=25s , $\tau_{t,int}$=5s and τ_s=3s

Figure 19 shows the average latent effectiveness errors from the hot (and humid) period and cold (and dry) period for different sensor arrangements (duct and exchanger sensors for FBRs with semi-sawtooth profile, and sensors exposed to FBR with sawtooth profile) versus H^*. The sensor with a sawtooth profile has average errors that are very close to zero (less than 0.005%) in all values of H^*as mentioned earlier. The average values of the duct and exchanger sensors ($0.5\times(\Delta\varepsilon_{L,ave})_{exchanger} + (\Delta\varepsilon_{L,ave})_{duct}$) are also presented in this figure. Since the exchanger and duct sensors have opposite effectiveness errors signs, their average can be used to determine the latent effectiveness (with ±5% error) when $H^*>1.6$ and $H^*<-1$, according to Fig.19. Such observation is valuable as test facilities (such as the one developed by Krishnan et al. (Krishnan et al. 2020)) can be built to measure latent effectiveness directly from the sensor measurements.

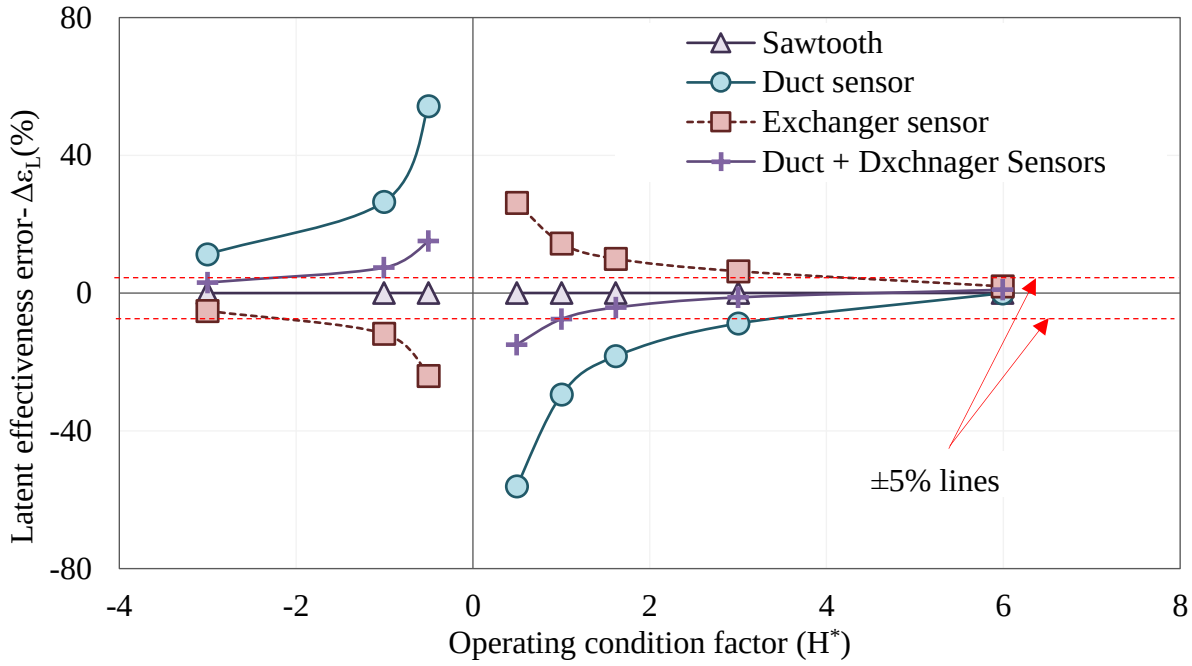

Figure 19. Average of the hot (and humid) and cold (and dry side) latent effectiveness errors for sensors exposed to sawtooth, and semi-sawtooth (exchanger and duct sensors) profiles and the average of latent effectiveness errors for duct and exchanger sensors

The effect of doubling all time constants on $\Delta\varepsilon_{L,ave}$ is presented in Fig. 20. $\Delta\varepsilon_{L,ave}$ remains very close to zero (less than 0.05%) for the sensors exposed to sawtooth profile over the range of H^*, which suggests that $\Delta\varepsilon_{L,ave}$ are independent of sensors transient characteristics for this types of FBRs. For the duct sensors, the absolute $\Delta\varepsilon_{L,ave}$ increases when sensor time constants doubles. The exchanger sensors absolute $\Delta\varepsilon_{L,ave}$ increase for negative H^* while decreases for positive H^* for doubling the sensors time constants. Further studies are required to understand the impact of sensor transient characteristics on effectiveness errors for the duct and exchanger sensors.

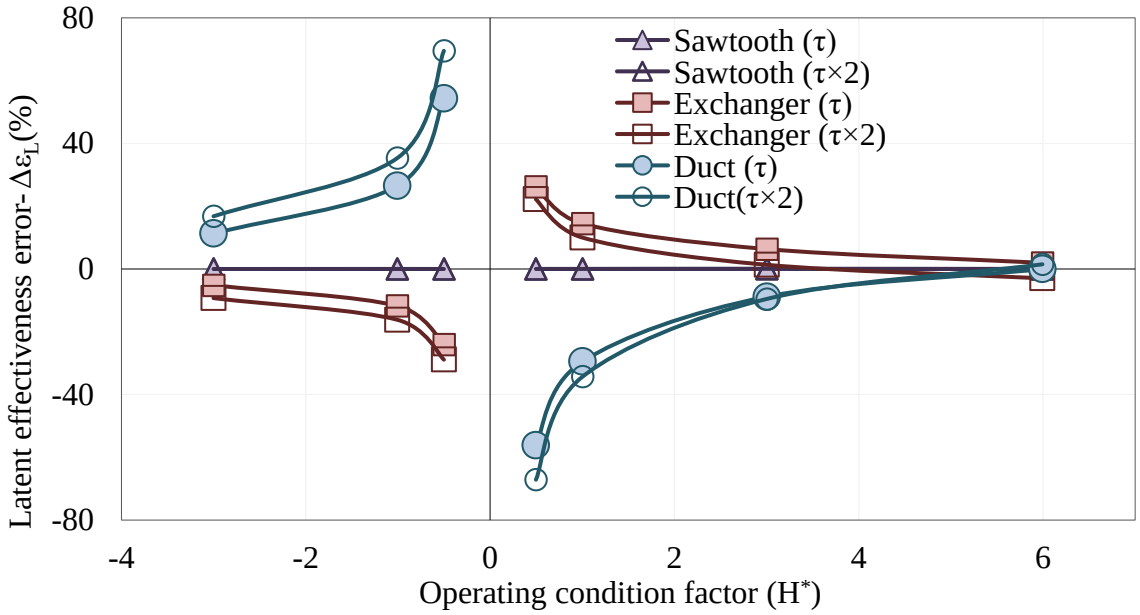

Figure 20. Comparison of the average effectiveness error for different sensor configurations with the original time constants ($\tau_{t,int}$=25s , $\tau_{t,int}$=5s and τ_s=3s) and when the original time constants are doubled ($\tau_{t,int}$=50s , $\tau_{t,int}$=10s and τ_s=6s).

7.4 Testing Standards

ASHRAE standard 84 (ASHRAE 2019) and CSA C439-18 standard (CSA Group 2018) do not distinguish between FBRs in terms of their air outlet properties profile, i.e., sawtooth and semi-sawtooth profiles. However, the current study results show that the measurement requirements for desiccant-coated FBRs depend on the shape of their outlet properties profile.

The average latent effectiveness on the dry and humid sides of FBRs with a sawtooth profile can be used as an accurate estimate for the latent effectiveness as found in this research regardless of the measurement sensor characteristics. Therefore, it can be concluded that the sensor requirements for FBRs with a sawtooth outlet profile in the standards could be relaxed. However, there is no simple recommendation for FBRs with semi-sawtooth outlet profiles; rather, the latent effectiveness error depends on the location of sensors, sensor transient characteristics, design, and operating conditions. Thus, further studies are required before recommendations can be made on the requirements of the sensor for FBRs with semi-sawtooth outlet profiles.

The temperature sensor requirements for sensible effectiveness in the testing standards are available in the literature (Ramin et al. 2021), indicating that the temperature sensor requirements in standards are stringent and could be relaxed for FBRs with sawtooth outlet temperature profiles. For FBRs with semi-sawtooth profiles, the temperature sensor should be carefully chosen from available tables and graphs to avoid measurements errors (Ramin et al. 2021). However, the standard requirement is still conservative for FBR with semi-sawtooth profiles.

The previous study also verified the experiment duration to reach a quasi-steady-state condition in standards for sensible FBRs (Ramin et al. 2020). However, further studies are required to verify quasi-steady-state experiment duration requirements for desiccant-coated FBRs.

8 Conclusions

The properties (temperature and humidity ratio) of air streams at the outlet of the desiccant-coated FBRs vary with time, which poses difficulties for sensors to accurately measure the humidity and temperature changes during the operation of FBRs. In this paper, a numerical model consisting of an FBR model and sensor (temperature and humidity sensors) models has been developed and validated with experimental results from a small-scale test facility. The numerical

model can predict the latent effectiveness error due to the transient response of both the humidity and temperature sensors. It is found that the location of the sensors and the configuration of FBR affect the latent effectiveness error. Depending on configurations of FBR, air properties at the outlet of FBRs follow either sawtooth or semi-sawtooth profiles. There are two different sensor positions for the semi-sawtooth profile, i.e., exchanger sensor and duct sensor. Both the sawtooth and semi-sawtooth profiles were examined using the validated numerical model, and the following conclusions were obtained:

- The latent effectiveness error due to the transient nature of FBR and sensors depends on the design conditions, operating condition factor (H^*), and the characteristics of the sensors. The error in the measured effectiveness is smaller for FBR with a sawtooth profile than with semi-sawtooth profile. At higher H^* (small temperature and considerable moisture content differences between the inlets of FBR, i.e., $H^* \gg 1$ or ΔT_{inlet}=small, ΔW_{inlet}=large), the latent effectiveness error is small. However, at smaller H^* ($H^* \approx 0$ or ΔT_{inlet}=large, ΔW_{inlet}=small), the latent effectiveness error is considerably higher.
- For FBRs with a sawtooth profile, the latent effectiveness error on the humid (and hot) and dry (and cold) sides are equal but with the opposite sign. Thus, the effectiveness can be obtained by averaging the effectiveness values from both sides of the FBR. The ASHRAE standard 84 and CSA C439-18 standard test configurations produce sawtooth profiles at the outlet of FBRs, and accurate measurement of latent effectiveness is possible by averaging the dry and humid sides of FBR.
- For FBRs with semi-sawtooth profiles, the effects of sensor response time and position are significant in the effectiveness evaluation. Also, the dry (and cold) and humid (and hot) sides of the desiccant-coated FBR have different latent effectiveness errors. For these types

of desiccant-coated FBR, careful consideration is required to choose the proper measurement instrumentations.

- The ASHRAE standard 84 and CSA C439-18 standard recommendation for sensor characteristics (response time shorter than 2 seconds for FBR with 60s recovery period) at the outlet of FBR with the sawtooth profile are rigorous and could be relaxed while still maintaining acceptable uncertainty limits.

Further studies are required to quantify the impact of different parameters on the latent effectiveness measurements for the desiccant-coated FBRs with semi-sawtooth profiles, which is the topic of future studies. The results of the current study will be helpful to develop the measurement recommendations for the future versions of ASHRAE standard 84 and CSA C439-18 standards for testing the desiccant-coated FBRs.

ACKNOWLEDGMENTS

Financial support from the College of Engineering and College of Graduate and Postdoctoral Studies (CGPS) of the University of Saskatchewan, ASHRAE support from Graduate Grant In Aid, Natural Science and Engineering Research Council (NSERC), Canada, and Tempeff North America Inc., Winnipeg, Canada (Project No: 533225-18) are gratefully acknowledged.

References

Abe, Oyetope O., Robert W. Besant, Carey J. Simonson, and Wei Shang. 2006. "Relationship between Energy Wheel Speed and Effectiveness and Its Transient Response, Part I: Mathematical Development of the Characteristic Time Constants and Their Relationship with Effectiveness." In *ASHRAE Transactions*, 112:89–102.

Aristov, Yu A., I. V. Mezentsev, and V. A. Mukhin. 2006. "A New Approach to Heat and Moisture Regeneration in the Ventilation System of Rooms. I. Laboratory Prototype of the Regenerator." *Journal of Engineering Physics and Thermophysics* 79 (3): 569–76. https://doi.org/10.1007/s10891-006-0137-7.

ASHRAE. 2012. *HVAC Systems and Equipment, ASHRAE Handbook,* Altanta, GA, USA.

———. 2019. *BSR/ASHRAE Standard 84-2013R, Method of Testing Air-to-Air Heat/Energy Exchangers (First Public Review Draft)*. Atlanta, GA, USA.

Bergman L., Theodore, Adrinne Lavine S., Frank P Incropera, and David P DeWitt. 2011. *Fundamentals of Heat and Mass Transfer*. Seveneth e. John Wiley & Sons, INC. https://doi.org/10.1016/j.applthermaleng.2011.03.022.

Borodulin, V. Yu, and M. I. Nizovtsev. 2018. "A Criterial Analysis of the Effectiveness of Air-to-Air Heat Exchangers with Periodic Change of Airflow Direction." *Applied Thermal Engineering* 130: 1246–55. https://doi.org/10.1016/j.applthermaleng.2017.11.126.

Cerrah, Ecem, Claire McCague, and Majid Bahrami. 2020. "Sorbent Based Enthalpy Recovery Ventilator." *Energy and Buildings* 211. https://doi.org/10.1016/j.enbuild.2020.109755.

Chang, Chih Chung, Sih Li Chen, Tzu Yuan Lin, and Yuan Ching Chiang. 2017. “Experimental and Theoretical Investigation of Regenerative Total Heat Exchanger with Periodic Flow for Air-Conditioning Systems.” *International Journal of Refrigeration* 81: 123–33. https://doi.org/10.1016/j.ijrefrig.2017.05.015.

Chang, Chih Chung, Ching Hsien Lai, Cheng Min Yang, Yuan Ching Chiang, and Sih Li Chen. 2013. “Thermal Performance Enhancement of a Periodic Total Heat Exchanger Using Energy-Storage Material.” *Energy and Buildings* 67: 579–86. https://doi.org/10.1016/j.enbuild.2013.08.061.

Chang, Chih Chung, Jyun De Liang, and Sih Li Chen. 2018. “Performance Investigation of Regenerative Total Heat Exchanger with Periodic Flow.” *Applied Thermal Engineering* 130: 1319–27. https://doi.org/10.1016/j.applthermaleng.2017.11.024.

CSA Group. 2018. *CSA C439 Standard Laboratory Methods of Test for Rating the Performance of Heat / Energy-Recovery*. Toronto, ON, Canada, CSA Group.

Diao, Yanhua, Ji Zhang, Wenjing Yu, and Yaohua Zhao. 2014. “Experimental Study on the Heat Recovery Characteristic of a Plate Heat Pipe Heat Exchanger in Room Ventilation.” *HVAC&R Research* 20 (7): 828–35. https://doi.org/10.1080/10789669.2014.945852.

Dooley, J. Brandon, and Dennis L. O’Neal. 2008. “The Transient Response of Capacitive Thin-Film Polymer Humidity Sensors.” *HVAC and R Research* 14 (5): 663–82. https://doi.org/10.1080/10789669.2008.10391033.

Fan, Haisheng, Carey J. Simonson, Robert W. Besant, and Wei Shang. 2006. “Performance of a Run-around System for HVAC Heat and Moisture Transfer Applications Using Cross-Flow

Plate Exchangers Coupled with Aqueous Lithium Bromide." *HVAC&R Research* 12 (2): 313–36. https://doi.org/10.1080/10789669.2006.10391181.

Figliola, Richard S., and Donald E. Beasley. 2010. *Theory and Design for Mechanical Measurements*. 5th ed. New Jersey: John Wiley & Sons Inc, Hoboken. https://doi.org/10.1017/CBO9781107415324.004.

Hashemian, HM. 2011. "Measurement of Dynamic Temperatures and Pressures in Nuclear Power Plants." PhD thesis, The University of Western Ontario. http://ir.lib.uwo.ca/etd/189/.

Kaplya, V. I., E. V. Kaplya, and A. A. Silaev. 2020. "Identification of the Transient Response of a Capacitive Relative Humidity Sensor." *Measurement Techniques* 62 (12): 1099–1105. https://doi.org/10.1007/s11018-020-01740-0.

Kassai, Miklos. 2018. "Experimental Investigation of Carbon Dioxide Cross-Contamination in Sorption Energy Recovery Wheel in Ventilation System." *Building Services Engineering Research and Technology* 39 (4): 463–74. https://doi.org/10.1177/0143624417744733.

Krishnan, Easwaran N., Hadi Ramin, A. Gurubalan, and Carey J. Simonson. 2022. "Experimental Methods to Determine the Performance of Desiccant Coated Fixed-Bed Regenerators (FBRs)." *International Journal of Heat and Mass Transfer* 182: 121909. https://doi.org/10.1016/j.ijheatmasstransfer.2021.121909.

Krishnan, Easwaran N., Hadi Ramin, Mohsen Shakouri, Lee D. Wilson, and Carey J. Simonson. 2020. "Development of a Small-Scale Test Facility for Effectiveness Evaluation of Fixed-Bed Regenerators." *Applied Thermal Engineering* 174 (June): 115263. https://doi.org/10.1016/j.applthermaleng.2020.115263.

Krishnan, Easwaran N., Hadi Ramin, and Carey J Simonson. 2019. “Performance Testing of Fixed-Bed Regenerators for Hvac Applications.” In *The Second Pacific Rim Thermal Engineering Conference*, pp.1–5. Hawaii, USA, Decmber 13-17.

Lowenstein, Andrew. 2008. “Review of Liquid Desiccant Technology for HVAC Applications.” *HVAC&R Research* 14 (6): 819–39. https://doi.org/10.1080/10789669.2008.10391042.

Mathworks-Inc. 2019. “MATLAB: 2019b.” Natick, Massachusetts.

Nizovtsev, M. I., V. Yu Borodulin, V. N. Letushko, and A. A. Zakharov. 2016. “Analysis of the Efficiency of Air-to-Air Heat Exchanger with a Periodic Change in the Flow Direction.” *Applied Thermal Engineering* 93: 113–21. https://doi.org/10.1016/j.applthermaleng.2015.09.029.

Ramin, Hadi, Easwaran N. Krishnan, Gurubalan Annadurai, Wahab O. Alabi, and Carey J. Simonson. 2021. “Transient Sensor Errors and Their Impact on Fixed-Bed Regenerator (FBR) Testing Standards.” *Science and Technology for the Built Environment* 27 (5): 656–78. https://doi.org/10.1080/23744731.2020.1846428.

Ramin, Hadi, Easwaran N. Krishnan, Gurubalan Annadurai, and Carey J. Simonson. 2020. “Transient Performance of Fixed-Bed Regenerators for Energy Recovery in Building Applications.” In *ASME 2020 Heat Transfer Summer Conference*. Orlando, Florida: ASME. https://doi.org/10.1115/HT2020-9057.

Ramin, Hadi, Easwaran N. Krishnan, A. Gurubalan, Wahab O. Alabi, and Carey J. Simonson. 2021. “A Transient Numerical Model for Sensible Fixed-Bed Regenerator in HVAC Applications.” *International Journal of Heat and Mass Transfer* 177: 121550.

https://doi.org/10.1016/j.ijheatmasstransfer.2021.121550.

Ramin, Hadi, Easwaran N. Krishnan, and Carey J. Simonson. 2020. “Effectiveness of Fixed-Bed Regenerators for Energy Recovery in Buildings Applications.” *E3S Web of Conferences* 172: 1–8. https://doi.org/10.1051/e3sconf/202017209001.

Ramin, Hadi, Eswaran N. Krishnan, and Carey J. Simonson. 2019. “Fixed Bed Regenerators for HVAC Applications.” In *27th Canadian Congress of Applied Mechanics*, 1–6. Sherbrooke, Québec, Canada: MDPI. https://doi.org/10.3390/proceedings2019023004.

Ramin, Hadi, Easwaran N. Krishnan Wahab Alabi, and Carey J. Simonson. 2020. “Temperature Measurement Correction for the Determination of the Effectiveness of Fixed-Bed Regenerators (FBRs) for HVAC Applications.” In *ASHRAE Transactions*, 126:366–74. Austin: ASHRAE.

Simonson, C. J., and R. W. Besant. 1999. “Energy Wheel Effectiveness: Part I-Development of Dimensionless Groups.” *International Journal of Heat and Mass Transfer* 42 (12): 2161–70. https://doi.org/10.1016/S0017-9310(98)00325-1.

Simonson, Carey J. 1998. “Heat and Moisture Transfer in Energy Wheels.” PhD thesis, University of Saskatchewan.

Simonson, Carey J., and R. W. Besant. 1999a. “Energy Wheel Effectiveness: Part I-Development of Dimensionless Groups.” *International Journal of Heat and Mass Transfer* 42 (12): 2161–70. https://doi.org/10.1016/S0017-9310(98)00325-1.

———. 1999b. “Energy Wheel Effectiveness: Part II-Correlations.” *International Journal of*

Heat and Mass Transfer 42 (12): 2171–85. https://doi.org/10.1016/S0017-9310(98)00327-5.

Simonson, Carey J., and Robert W. Besant. 1997a. “Heat and Moisture Transfer in Desiccant Coated Rotary Energy Exchangers: Part I. Numerical Model.” *HVAC and R Research* 3 (4): 351–68. https://doi.org/10.1080/10789669.1997.10391382.

———. 1997b. “Heat and Moisture Transfer in Desiccant Coated Rotary Energy Exchangers: Part II. Validation and Sensitivity Studies.” *HVAC and R Research* 3 (4): 351–68. https://doi.org/10.1080/10789669.1997.10391382.

Tempeff North America. 2020. “Heat Recovery System | Heat Recovery Ventilator | ERV | Energy Recovery.” 2020. https://www.tempeffnorthamerica.com/.

Vaisala. 2019. “Response Time in Humidity Measurement.” *Technical Note*, 2. www.vaisala.com/contactus.

Versteeg, H K, and W Malalasekera. 2007. *An Introduction to Computational Fluid Dynamics*. *AIAA Journal*. Second Edi. Vol. 44. Essex: Pearson Education Limited. https://doi.org/10.2514/1.22547.

Wallin, Jörgen, Hatef Madani, and Joachim Claesson. 2012. “Run-around Coil Ventilation Heat Recovery System: A Comparative Study between Different System Configurations.” *Applied Energy* 90 (1): 258–65. https://doi.org/10.1016/j.apenergy.2011.05.012.

Wang, S., Juming Tang, and F. Younce. 2003. “Temperature Measurement.” In *Encyclopedia of Agricultural, Food, and Biological Engineering*, 987–93. New York: Marcel Dekker, Inc.

https://doi.org/10.1081/E-EAFE.

Wang, Yiheng, Robert W. Besant, Carey J. Simonson, and Wei Shang. 2006. “Application of Humidity Sensors and an Interactive Device.” *Sensors and Actuators, B: Chemical* 115 (1): 93–101. https://doi.org/10.1016/j.snb.2005.08.038.

Wang, Yiheng, Carey J. Simonson, Robert W. Besant, and Wei Shang. 2007a. “Transient Humidity Measurements: Part I - Sensor Calibration and Characteristics.” *IEEE Transactions on Instrumentation and Measurement* 56 (3): 1074–79. https://doi.org/10.1109/TIM.2007.894881.

———. 2007b. “Transient Humidity Measurements: Part II - Determination of the Characteristics of an Interactive Device.” *IEEE Transactions on Instrumentation and Measurement* 56 (3): 1080–86. https://doi.org/10.1109/TIM.2007.894882.

Wemhoener, Carsten, Werner Hässig, Sara Wyss, and Jan Staubli. 2016. “Heat Pump Application in Nearly Zero Energy Buildings.” *Science and Technology for the Built Environment* 23 (4): 637–50. https://doi.org/10.1080/23744731.2016.1239467.